Available online at www.sciencedirect.com
ScienceDirect
ELSEVIER
C. R. Physique 7 (2006) 1046–1072
COMPTES RENDUS
PHYSIQUE
http://france.elsevier.com/direct/COMREN/

Nucleation/Nucléation

Role of patterning in islands nucleation on semiconductor surfaces

Nunzio Motta [a,*], Pierre D. Szkutnik [b], Massimo Tomellini [c], Anna Sgarlata [d], Massimo Fanfoni [d], Fulvia Patella [d], Adalberto Balzarotti [d]

[a] *School of Engineering Systems, Queensland University of Technology, GPO Box 2434, Brisbane 4001, Australia*
[b] *L2MP – CNRS, umr 6137, Faculté des Sciences de St Jérôme, Avenue Escadrille Normandie niemen – case 142, F-13397 Marseille cedex 20, France*
[c] *Dipartimento di Chimica, Università di Roma Tor Vergata, Via della Ricerca Scientifica 1, 00173 Roma, Italy*
[d] *Dipartimento di Fisica, Università di Roma Tor Vergata, Via della Ricerca Scientifica 1, 00173 Roma, Italy*

Abstract

Quantum dots (QDs) grown on semiconductors surfaces are actually the main researchers' interest for applications in the forthcoming nanotechnology era. New frontiers in nanodevice technology rely on the precise positioning of the nucleation site and on controlling the shape and size of the dots. In this article we will review some recent studies regarding the control of the nucleation process on semiconductor surfaces. A few approaches to form ordered patterns on surfaces are described: natural patterning induced by surface instabilities (as step bunching or step meandering), in situ substrate patterning by Scanning Tunneling Microscopy (STM), high resolution patterning by Focused Ion Beam (FIB). Growth of epitaxial layers of semiconductors (Ge/Si(100) and InAs/GaAs(100)) on patterned surfaces has been studied by STM or Atomic Force Microscopy (AFM) unveiling the way in which the first atoms start to aggregate and identifying their exact nucleation site. Control of the dot size to match the patterning typical wavelength has been achieved by using surfactants on misoriented substrates. STM images acquired in real time allows one to identify the mechanism of Ge cluster formation on patterned Si(100), and to follow the island transition from pre-pyramid to pyramid. Nucleation of ordered Ge dots on SiO_2 substrates has been obtained thanks to FIB tight patterning, achieving island densities of $3.5 \times 10^{10}/\text{cm}^2$. ***To cite this article: N. Motta et al., C. R. Physique 7 (2006).***
© 2006 Académie des sciences. Published by Elsevier Masson SAS. All rights reserved.

Résumé

Rôle de la structuration lors de la nucléation d'îlots sur les surfaces des semi-conducteurs. Les boîtes quantiques (BQ) obtenues par croissance sur les surfaces des semi-conducteurs constituent l'objectif prioritaire des chercheurs en vue de développer de nouvelles applications technologiques dans les prochaines années. Les nouvelles perspectives dans la technologie des nanodispositifs reposent sur un positionnement précis du site de nucléation des BQs et sur le contrôle de leur forme et de leur taille. Dans le présent article, nous passerons en revue quelques études récentes concernant le contrôle de la nucléation sur les surfaces des semi-conducteurs. Après un bref rappel de la théorie de la nucléation « libre » sur les surfaces et sur le rôle des marches et des défauts, on explore quelques voies nouvelles pour former des structurations ordonnées : d'une part une structuration naturelle induite par des instabilités de surface (par exemple mise en paquet des marches ou formation de méandres sur les marches), d'autre part une structuration in situ du substrat par microscopie à effet tunnel (STM), et une structuration à haute résolution par faisceaux d'ions focalisés (FIB). La croissance des couches épitaxiales de semi-conducteurs (Ge/Si(100) et InAs/GaAs(100)) sur ces surfaces à morphologie structurée a été étudiée par STM ou Microscopie à Force Atomique (AFM), révélant le mode d'agrégation

* Corresponding author.
E-mail address: n.motta@qut.edu.au (N. Motta).

1631-0705/$ – see front matter © 2006 Académie des sciences. Published by Elsevier Masson SAS. All rights reserved.
doi:10.1016/j.crhy.2006.10.013

des premiers atomes et identifiant le site exact de la nucléation. Par l'emploi de surfactants sur substrats désorientés, on a induit une taille de BQs, afin qu'elles s'adaptent à la longueur d'onde typique de la structuration. Les images STM, obtenues en temps réel, ont permis d'identifier le mécanisme de formation des agrégats de Ge sur Si(100) présentant une structuration morphologique spécifique, et de suivre la transition des îlots de la forme pré-pyramidale à la forme pyramidale. Le contrôle du site de nucléation des îlots de Ge sur les couches de SiO_2 a été obtenue par FIB, permettant d'obtenir des densités d'îlots de $3{,}5 \times 10^{10}/\mathrm{cm}^2$. ***Pour citer cet article : N. Motta et al., C. R. Physique 7 (2006).***
© 2006 Académie des sciences. Published by Elsevier Masson SAS. All rights reserved.

Keywords: Quantum dots; Nucleation process; Semiconductor surfaces

Mots-clés : Boîtes quantiques ; Contrôle de la nucléation ; Surfaces des semi-conducteurs

1. Introduction

The assembly of ordered nanostructures on semiconductor surfaces is a subject of active experimental and theoretical research [1–3]. This interest is due to the self-organization of three-dimensional (3D) quantum dots in SiGe [4–7], III–V [8–16] and II–VI systems [17] which derives from the complex nature of the nucleation process. Great efforts are devoted to elucidating island nucleation and evolution mechanisms. Nucleation is a really crucial point, since the possibility to create ordered and hence homogeneous array of islands stems from their exact and regular positioning on a surface. Island formation occurs by different stages. Mo et al. [18], Vailionis et al. [19], Goldfarb et al. [20] and Tersoff et al. [3] have observed the existence of embryos before the formation of Ge hut clusters and Voigtländer [7] has examined the metastable nature of these embryos and the asymmetric evolution of the resulting pyramids. However, the reason of the growth of these embryos is still under debate, and no control has been achieved on natural surfaces. In this article we will give an overview of some issues connected to nucleation, and set them in the context of the growth of islands on semiconductor surfaces. We will start from the general theory of nucleation and describe the nucleation in various morphological conditions: flat surfaces, steps, step-bunching, vicinal surfaces, holes, patterned surfaces. We have been able to analyze the details of the nucleation process and to follow the growth in real time thanks to the power of the Scanning Probe Microscopy [21], which yields atomic resolution topography of surfaces in Ultra High Vacuum. Especially useful to this purpose is the set up developed by Voigtländer [7] that allows the acquisition Scanning Tunneling Microscopy images during epitaxy, thanks to a smart design of the apparatus. A similar design has been developed by Omicron GmbH, and implemented in the VT series; one of these microscopes has been installed in the Roma Tor Vergata University, and has allowed our group to study in detail the nucleation and growth of, in particular, Ge/Si and InAs/GaAs islands.

2. Nucleation on surfaces

Nucleation is the first step of film formation at solid surface. It takes place when a certain number of diffusing adatoms cluster to form a nucleus. The latter, once having reached a critical size, has the same chance to grow as to decay. The growth proceeds by incorporation of monomers into stable nuclei or islands. We do not intend here to search into the subject of nucleation, because other chapters of this issue are explicitly devoted to this end. Nevertheless, some results will be reviewed which can be of some help in the ensuing discussion.

Depending on the size of the critical nucleus the nucleation process can be described on either a thermodynamic or atomistic basis. In the thermodynamic approach the 'single' nucleus has to be a thermodynamic system that is made up of a large number of atoms. In this instance the free energy change for the formation of a nucleus, ΔG, is a meaningful concept and can be expressed in terms of chemical potential of components in the nucleus (vapour) phase and surface free energy. In the case of heterogeneous nucleation the following relation holds

$$\Delta G = -\sum_k \Delta\mu_k c_k V_c + S_{c,v}\sigma_{c,v} + S_{c,s}(\sigma_{s,c} - \sigma_{s,v}) \tag{2.1}$$

where V_c is the volume of the cluster, the subscripts s, c and v stand for substrate, cluster, and vapour phases respectively. S and σ denote the area and the surface free energy of the interface. c_k is the concentration of the k component

in the infinite crystal and $\Delta\mu_k$, also referred to as supersaturation, is defined as

$$\Delta\mu_k = \mu_{k(v)} - \mu_{k(s)} \tag{2.2}$$

where $\mu_{k(v)}$ and $\mu_{k(s)}$ are the chemical potentials of the k component in the vapour and solid phases, respectively. By treating the vapour as an ideal gas at pressure P and indicating with $P_{k(e)}$ the partial pressure of the k component in equilibrium with the infinitely large crystal phase, it can be shown that

$$\Delta\mu_k = k_B T \ln \frac{P y_k}{P_{k(e)}} \tag{2.3}$$

k_B being the Boltzmann constant and y_k is $P y_k / P_{k(e)}$ the molar fraction in the vapour phase (mother phase). On occasion, the supersaturation is simply referred to as $P y_k / P_{k(e)}$. As anticipated, a thermodynamic approach makes sense since it is possible to define the bulk and the surface free energies of the nucleus together with its radius. For instance, in the model case of the hemispherical nuclei the free energy displays a maximum at the critical radius

$$r^* = \frac{2\sigma_{c,v} v}{\overline{\Delta\mu}} \tag{2.4}$$

where $\overline{\Delta\mu} = \sum_k \Delta\mu_k x_k$, x_k is the molar fraction of the k component in the bulk solid and $v^{-1} = \sum_k c_k$. In Eq. (2.4) the Young–Dupré [22] relation has been used. Low supersaturation, which according to Eq. (2.3) put into words a quasi equilibrium condition, promotes a large critical nucleus. In turn, in the more general case of a spherical cap, the work necessary for the critical nucleus to grow is

$$\Delta G(r^*, \theta) = \Delta G^*_{\text{hom}} \phi(\theta) \tag{2.5}$$

where $\phi(\theta) = (1 - \cos\theta)^2 (2 + \cos\theta)/4$, θ being the wetting angle and $\Delta G^*_{\text{hom}} = 16\pi\sigma^3_{c,v} v^2 / 3\overline{\Delta\mu}^2$. Moreover, it is possible to demonstrate that the work of formation of the critical nucleus increases if the latter is strained elastically. The strain, typical of solid interfaces, is brought about by the lattice mismatch between the components making up the interface.

When the supersaturation becomes larger and larger the size of the critical nucleus falls drastically (few atoms) insomuch that it becomes impossible to attach a radius to it and, as a consequence, a surface and a volume. As a matter of fact, the only significant way to attack the problem is to make use of the atomistic approach which instead of the radius and the free energy takes into account the number of monomers making up the nucleus and their binding energies as well as the desorption and diffusion energies, i.e. the interaction of monomers with the substrate. The operative definition of critical nucleus is due to Walton [23] who assumed the existence of a sharp critical size (number of monomers) $n = i$ and stable clusters $n \geqslant i + 1$. He was able to determine the rate of nucleation, I, by using statistical mechanics in the case of a single component; his conclusion can be summarized as follows:

$$I = N_i \Gamma_i^+ \tag{2.6}$$

where $\Gamma_i^+ = \sigma_i N_1 a \nu \exp(-E_D / k_B T)$ is the rate at which single adatoms join the nucleus of size i, while $N_i = \frac{1}{a^2} (\frac{F a^2}{\nu})^i \exp[(i E_{\text{ad}} + E_i)/k_B T]$ is the number of critical nuclei of size i. Moreover, N_1 is the number of monomers, σ_i is the capture factor of the critical nucleus, a is the distance between two adsorption sites, ν is the attempt frequency, E_D is the barrier to adatom diffusion, F is the flux, E_{ad} is the adsorption energy, E_i is the energy to form a critical cluster.

Although many researchers gave fundamental contributions to the development of rate equation approach [24–26], Walton's theory was put into rate equation by Frankl and Venables [27,28]. They introduced the idea of stationary state for sub-critical nuclei. After Venables, rate equations for total condensation assume the form [28]

$$\begin{aligned}
\dot{n}_1 &= F - 2\sigma_1 D n_1^2 - D n_1 \sum_{j>1}^{i} \sigma_j n_j - \sigma_x D n_1 n_x \\
\dot{n}_j &= 0 \quad (2 \leqslant j \leqslant i) \\
\dot{n}_x &= D\sigma_i n_1 n_i - 2 n_x \dot{S}
\end{aligned} \tag{2.7}$$

where D is the diffusion coefficient of monomers, n_k is the concentration of clusters made up of k monomers, $n_x = \sum_{k \geqslant i+1} n_k$ is the concentration of stable clusters, S is the portion of surface occupied by stable clusters. The meaning

of any single term of Eq. (2.7) is evident: the number of monomers increases because of flux, while decreases due to the formation of dimers and to the capture of monomers from sub-critical and stable clusters. The concentration of stable clusters increases because monomers add to critical clusters and decrease because of coalescence among clusters. The latter process is taken into account by the last term on the right-hand side of the $\dot{n}_x$ equation according to Vincent's model [29]. It can be written in that form for small values of S, only. As a matter of fact, the monomer diffusion implies the existence of an area around each cluster in which nucleation is strongly depleted and consequently it entails a certain degree of spatial correlation among clusters. Fanfoni, Tomellini and Volpe [30] have proposed a rate equation scheme which takes into account the spatial correlation. They confined the analysis to the case of total condensation and stable dimer, however, the most important peculiarity is that, at variance with other contributions, their solution, thanks to a suitable treatment of the coalescence process, extends up to the film closure ($S = 1$). Although with different approaches, other researchers dealt with the question of how to introduce the correlation in a rate equation scheme [31,32]. Their model, broadly speaking, is centred on the calculation of the capture factor prior having determined the size distribution function of clusters which, in turn, is related to the Voronoi tessellation induced by clusters. In this contest it is worth noting that the above-mentioned rate equations do not allow for a reliable description of the size distribution function at least in the case of growth ruled by diffusion. In fact, according to Zinnsmeister [24], the mean field size distribution is found to be the mirror image of the kinetics of monomers. This kind of distribution is not in good agreement with those recently obtained by computer simulation, which are well described by the Gamma function. Nevertheless, rate equations have been shown to be successful in determining the mean quantities of the kinetics such as the nucleation density and average island size.

3. Role of steps and defects

A real surface is characterized by the presence of defects which act as preferential sites for nucleation. These defects can be randomly distributed or created in a controlled way, by using suitable tools like Focused Ion Beam [33], Electron Beam [34], Scanning Tunnelling Microscope [35], or other means. Also the distribution of steps on the surface can be controlled by realising ordered structures [36]. Under these circumstances rate equations have to be reassessed. In fact, if m is the number of point defects, under the hypothesis that the capture factors are independent of cluster size, a new set of rate equations can be written and solved in closed form [37]. They are

$$\begin{aligned} \dot{n}_1 &= F - wmn_1 - wn_1 n \\ \dot{n} &= wmn_1 \\ \dot{m} &= -wmn_1 \end{aligned} \tag{3.1}$$

where $w = \sigma D$ and satisfy to the initial condition $n(0) = 0$ and $m(0) = m_0 = n(t) + m(t)$ which derives from the conservation of nucleation sites. The solution of Eq. (3.1) reads

$$n(t) = m_0 \Big[1 - \mathrm{e}^{-\frac{Ft}{m_0}} \mathrm{e}^{\frac{Ft}{wm_0^2}(1-\mathrm{e}^{-wm_0 t})} \Big] \tag{3.2}$$

In [37] the system was numerically solved also by including the non-linear term n_1^2 that represents the intrinsic nucleation event, i.e. the dimer formation. The interplay between the two contributions to the overall nucleation has been investigated. The results are in agreement with the experimental evidence that nucleation at defects dominates, under typical conditions of growth as discussed in the following sections. Furthermore, inspection of Eq. (3.2) shows that for typical values of m_0, D and F, the kinetics reduces to

$$n(t) \approx m_0 \big(1 - \mathrm{e}^{-\frac{Ft}{m_0}} \big) \tag{3.3}$$

In fact, by considering $\sigma = 2$–3, $m_0 \approx 10^{12}\ \mathrm{cm}^{-2}$, $F = 10^{13}\ \mathrm{cm}^{-2}\,\mathrm{s}^{-1}$ a diffusion barrier of 0.2 eV and a diffusion pre-exponential factor of $10^{13}\ \mathrm{s}^{-1}$, one gets $\frac{F}{m_0^2 \sigma D} \approx 10^{-7}$.

4. Step bunching

Atomic steps are expected to act as nucleation sites for Ge islands, as reported, as an example, [38] on Si(111) mesas, but the step distribution on the surface affects strongly the island placement. Controlling the relative position

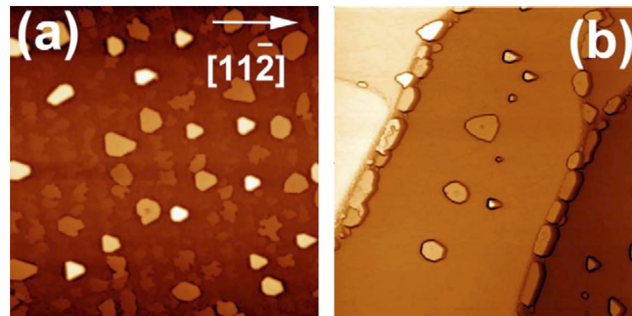

Fig. 1. Distribution of 3D Ge islands on different Si substrates. (a) STM topography $(3000 \times 3000 \times 29)\ \text{nm}^3$ on a R surface after 17 ML Ge deposition at $T = 723$ K; (b) STM topography $(2950 \times 3000 \times 73)\ \text{nm}^3$ on a SB surface after 8 ML Ge deposition at $T = 723$ K. The image has been enhanced by mixing the topography with the gradient image.

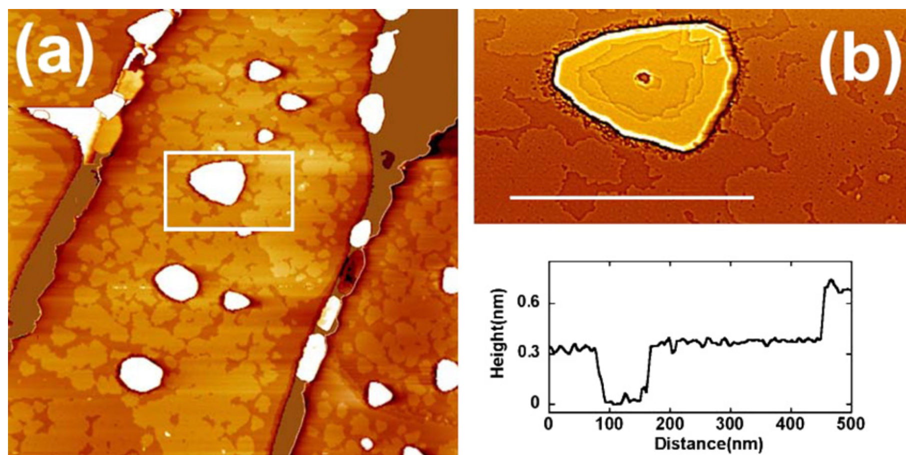

Fig. 2. (a) Color equalized image $(2850 \times 2850 \times 73)\ \text{nm}^3$ to enhance the roughness of the WL in (b); (b) Zoom $(920 \times 440 \times 8)\ \text{nm}^3$ of the marked area in (a) and profile taken along the white line.

of steps on the surface constitutes a route towards controlling island positioning. Also, since real surfaces are never step free, surfaces where step bunching occurs can mimic ideal flat surfaces if the terraces are wide enough (i.e. much larger than the mean diffusion length of an atom). We have obtained such a 'laboratory' on Si(111) substrates with miscut angles $<0.3°$, where terraces with variable width, ranging from 0.1 to 2 µm have been created by direct current heating via bunching of natural surface steps [39]. Several authors have studied this phenomenon [40–42], demonstrating that the step configuration at a vicinal surface depends on the direction of the current flowing through the steps, as well as on the miscut angle and on temperature [40,43]. With respect to the temperature dependence [44], for $T > 1493$ K, step bunching occurs in the step-down direction, while a regular step distribution occurs in the step-up direction.

We have studied the influence of surface morphology on the Stranski–Krastanov growth of Ge on both regular (R) and step-bunched (SB) Si(111) surfaces kept at 723 K [36].

We reported the evolution and distribution of the 3-dimensional (3D) islands that form after the completion of the Wetting Layer (WL), showing an evident self-ordering on SB surfaces. Ge was deposited at a substrate temperature of $T_s = 723 \pm 20$ K by Physical Vapor Deposition using a growth rate of about 0.3 ML/min on both SB and R surfaces.

Atomic steps are expected to act as nucleation sites for Ge islands, as reported [38] on Si(111) mesas, but the step distribution on the surface affects deeply the island placement. After depositing 17 ML of Ge on a R substrate, islands appear randomly distributed [7,45] (Fig. 1(a)).

By contrast, on SB substrates, islands first nucleate and evolve along step edges and only afterwards on flat terraces. Islands grown on step bunches undergo complete ripening. They are elongated and they coalesce, forming a continuous ribbon on SB [36]. When the evolution on the step edges is completed, nucleation takes place at the center of terraces (Fig. 1(b)). As evidenced by the color-equalised image (Fig. 2(a)) and by the zoom (Fig. 2(b)), the supercritically

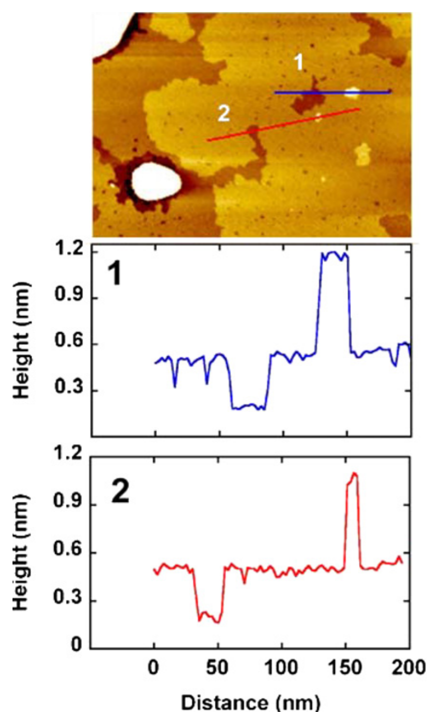

Fig. 3. Equalized image (564 × 358) nm^2 of a flat area close to the big island in Fig. 2(b). The blue (marked 1) and red (marked 2) profiles are taken to show the double layer height of island precursors. (See online version of this article for colours.)

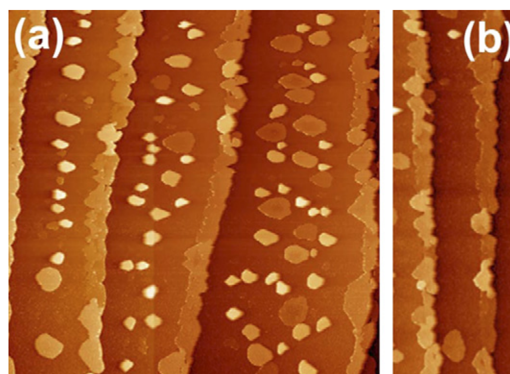

Fig. 4. (a) STM topography (10 000 × 10 000 × 30) nm^3 on a SB surface after 19 ML Ge deposition at $T = 450\,^\circ\mathrm{C}$; (b) STM topography (2660 × 10 000 × 12) nm^3 of an island-free terrace on the same sample as (a).

thick WL appears to roughen as a consequence of the metastable strained state before the 2D–3D transition [46]. In the central part of the terrace the WL is made of regions of overgrown areas typically one bi-layer high (Fig. 3(a)), whereas along the decorated edges, the WL shows a depleted region caused by the material that migrated towards the steps.

We have shown two little island precursors (two bi-layers high) randomly nucleated on the terrace marked by 1 and 2. The line profiles show this height difference. As suggested by Voigtlander [47] we believe that this kind of precursors are continually created and destroyed on the surface, until a suitable place with the right conditions of strain and atomic density is reached. This is consistent with the idea that, due to intermixing [48], the compressed Ge is more mobile [49] even without actually melting [8].

By increasing Ge coverage, step bunches appear fully decorated, the islands' size on terraces increases (Fig. 4(a)), and their density appears to be constant. Moreover, some flat, narrow terraces are found free of islands (Fig. 4(b)).

To quantify the lateral ordering of islands we have performed a statistical analysis of island-island and island-step-bunch distances. At a coverage of 8 ML [36] the average island-island distance is 360 ± 10 nm. The two distributions of island-step bunch distances (from upper and lower bunches) were fitted using two Gaussian peaks located at 470 ± 20 nm for the island-upper bunch and at 520 ± 20 nm for the island-lower bunch distribution, respectively. Each peak gives the minimal distance from the step at which island nucleation takes place. As a consequence, by summing these two distances, we can estimate the maximum width ($w_{\mathrm{depl}} \approx 1$ μm) for an island-free terrace, caused by the adatom attraction towards step borders.

On a SB surface covered by 19 ML of Ge and varying terrace widths we have measured both the island–island distance and the radial distribution function around each island (on each terrace). Values of 370 ± 10 nm for the island–island distance and of 340 ± 10 nm between nearest neighbors and next nearest neighbors islands are found, showing that the island–island distance is nearly constant. This result implies that the density of ordered islands is constant, as previously reported for Ge deposition on patterned Si(001) mesas [50]. Thus, we expect that few rows of

islands should form depending on the terrace width [51]. This is strikingly apparent in Fig. 4(a): a single row forms on a 2.1 μm wide terrace while a double row forms on a wider terrace (2.8 μm). In this way we have shown the possibility to change the number of island rows by tuning the terrace width. In fact, on terraces smaller than 1.2 μm, islands do not nucleate, as shown in Fig. 4(b). This value agrees with the previous estimate (1 μm) for the width of island-free terraces and its half (0.5 μm) is an upper limit of the diffusion length of Ge ad-atoms on Si(111) surfaces at 723 K.

5. Step meandering

The ability to grow crystalline materials with single-layer control down to the atomic scale is a central feature of advanced growth techniques such as molecular beam epitaxy (MBE). In epitaxial growth, atomic steps on the surface are of crucial importance since they can trigger kinetic instabilities producing coarsened final surfaces.

Burton, Cabrera and Frank introduced first the concept of step flow instability giving rise to step bunching of vicinal orientations [52]. In their one-dimensional model the 'velocity' of a straight-edge step (or terrace) is an increasing function of the width of the terraces in front and behind the step; this is due to the increased area for adatom exchange between the terrace and the vapor phase. For terraces whose widths are lower than the diffusion length of adatoms, the velocity increases to a maximum value and then saturates. In this case, a stable step-flow regime is set up and crystal growth proceeds predominantly by the motion of fairly straight and uniformly spaced train of steps. However, in some cases the uniform step system becomes kinetically unstable giving rise to a complex surface morphology made of bunches of steps and/or meandered step edges with fingerlike shapes often forming a highly connected network. The key feature producing kinetic instability is the asymmetry in the attachment rate of adatoms on the lower and higher terrace of the step, by which adatoms diffusing on the surface acquire a systematic drift perpendicular to the direction of step-edges (up-hill/down-hill current). Different mechanisms can account for this, some of which embody an extra diffusion-barrier for over-edge hopping, the Schwoebel barrier [53], giving rise, in most cases, to preferential attachment from the lower terrace.

The meandering of step edges results from the combined effect of the adatom density and the step morphology at the growing terrace. In particular, a protrusion of an upper terrace increases the local adatom density at the lower terrace and decreases the density at the upper terrace. From the surface diffusion equation it follows that if the adatom mobility toward steps is different at the upper and lower terrace this density inhomogeneity enhances the protrusion and the step edge meanders.

Many models have been developed which consider various non-equilibrium effects on the diffusion current in presence of steps [54–57]. One possible mechanism was first suggested by Frank [58], who argued that the adsorption of an impurity on the surface could lead to step bunching by hampering the motion of the step segment immediately behind it. This idea has been further developed by other researchers using more general 2D models, suitable to describe large scale morphologies, that allowed meandering of the step edges [59] by structures created during growth or evaporation that served as 'effective impurities'.

A picture of kinetically unstable growth is given by the AFM images of Fig. 5 which refer to 1.3 ML of InAs deposited by MBE on a GaAs(001) substrate. At this coverage InAs forms an alloyed strained 2D wetting layer on GaAs (7% lattice misfit). Although the (001) surface of GaAs is ideally flat, the real surface contains a low density of pre-existing steps due to the typical $\pm 0.1^{\circ}$ orientation miscut of the substrate; these steps can drive to kinetic growth instabilities of the (001) GaAs substrate. Bunching and meandering of steps of the substrate can be further enhanced in the growth of the InAs wetting layer where intermixing (In–Ga-exchange) and In segregation could act as a density of 'effective impurities'. At large-scales, Fig. 5(c), the surface consists of mounds, of approximately $1.2 \times 0.3\ \mu m^2$ size, having major axis in the $[1\bar{1}0]$ direction. On a mesoscopic scale, mounds are revealed to be bunches of meandered steps where long parallel terrace edges run along the [110] direction, while finger-like elongations align to the $[1\bar{1}0]$. At the very beginning the InAs wetting layer grows by step-flow and nucleation of 2D islands [60], at distances from step edges of the order of the cation migration length, as, for instance, in Fig. 5(a). At increasing depositions, up to 1.3–1.4 ML, the coalescence of 2D islands gives rise to additional terraces, nearing of steps and prevailing step-flow growth, as on vicinal surfaces. The distance between steps in the bunch progressively decreases from $\sim$120 nm up to a minimum of 40 nm, regardless of the original substrate miscut (Fig. 5(b)). The observation of a minimum distance or, equivalently, of a steady-state velocity of the step-train, accords with instability models that exclude energetically costly overhangs and step crossing [55].

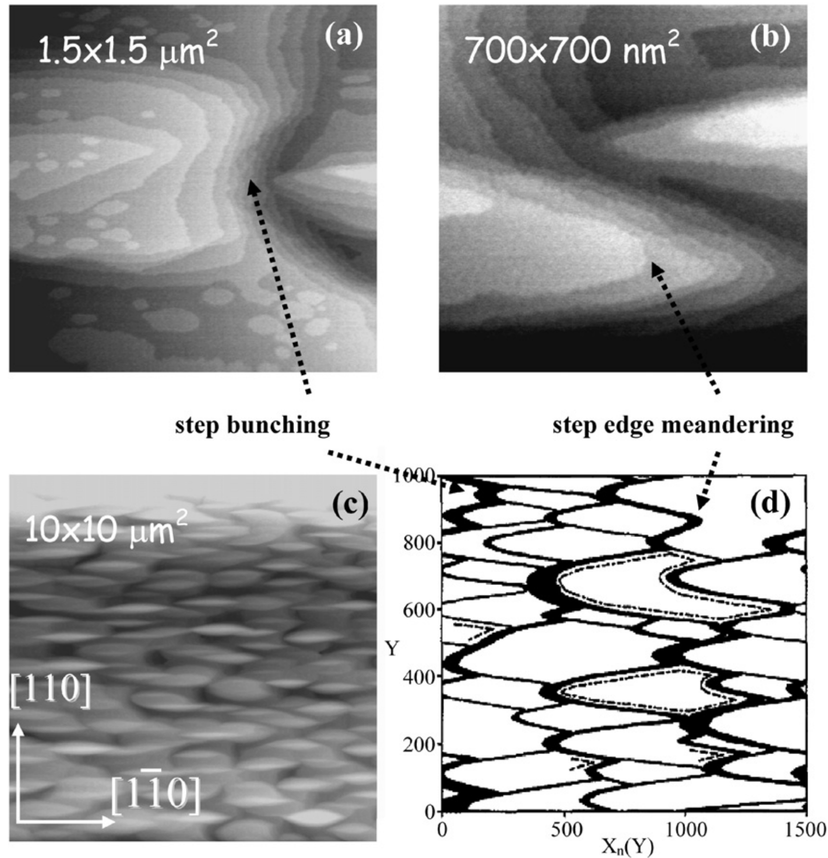

Fig. 5. AFM topographies of about 1.3 ML of InAs deposited on the GaAs(001) substrate: (a) 1.5×1.5 μm^2 image showing bunching of steps and nucleation of 2D islands on terraces; (b) 0.7×0.7 μm^2 image showing meandering of steps and finger-like elongations in the [1$\bar{1}$0] direction; (c) large scale image, 10×10 μm^2, where mounds, 1.2 μm × 0.3 μm wide and about 3 nm high, are aligned along the [1$\bar{1}$0]; (d) figure adapted from [59], showing the numerical simulation of a step-train instability. Steps, moving from left to right, are marked by solid lines. Heavy solid lines correspond to step-bunches.

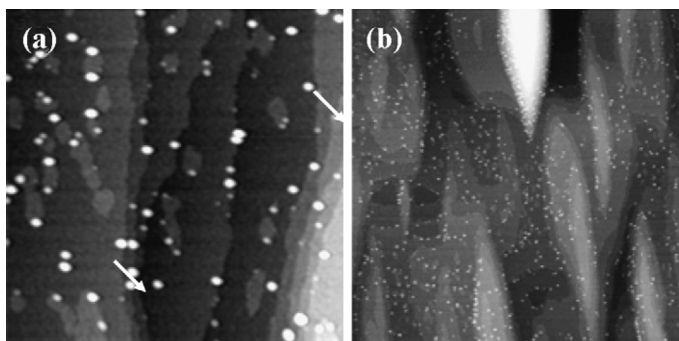

Fig. 6. InAs QD arrays on GaAs(001). 800×800 nm^2 AFM images of (a) 1.5 ML and (b) 1.7 ML of InAs on GaAs(001) where decoration of step edges by QDs is evident. Arrows indicate small 3D islands at the initial stage of nucleation which rest on the upper edge of steps. Mature 3D dots lie on the lower step edges.

Above 1.5 ML, InAs growth on GaAs(001) undergoes a 2D–3D transition of the Stranski–Krastanov type. Coherent islands, i.e. quantum dots (QD), form upon elastic-energy relaxation of the highly strained InAs layers. The self-assembling of QD, and, in particular, the lateral ordering, is largely dictated by the morphology of the wetting layer, as clearly seen in Fig. 6.

In Fig. 6(a) it is evident that the process begins with the nucleation of very small 3D islands (indicated by arrows) at the upper edge of steps and large 2D-islands.This fact indicates the presence of a minimum in the potential in proximity of the step edge caused by the readjustment of InAs atoms to lower the lattice misfit with the GaAs. The decoration of step-edges by dots clearly evidences the constraint on the lateral ordering induced by the substrate morphology dominated by bunching and meandering of steps.

6. Vicinal surfaces

Heteroepitaxy on vicinal semiconductor surfaces gives rise to growth instabilities [61,62], which can be used as natural nano-template. In the case of Ge growth on low miscut Si(001) surfaces, different mechanisms have been proposed as being responsible for such instabilities as strain-induced step bunching [63], step-edge barriers [64] and kinetic effects [65] such as diffusion anisotropy [66]. At high miscut, a complex situation is found where the interplay between the incorporation of adatoms, surface reconstruction, miscut azimuth and growth conditions result in a periodic surface corrugation, i.e. a rippled morphology [62,66–71]. This rippled morphology is able to relieve the strain and no islands are formed, because the ripples are actually infinitely long islands. At mesoscopic level, the ripples appear elongated perpendicularly or parallel to the miscut direction, depending whether the miscut angle is lower or larger than 4–6° [71,72]. In principle, strain release via step bunching should dominate due to the high density of steps. For instance, in corrugated Si layers with 4° miscut angle, strain relaxation is achieved by the coalescence of step bunches to form ridge structures oriented along the miscut direction with two low energy {105} facets inclined 8° with respect to the (001) plane [67].

To investigate the details of the formation of these structures we have performed a series of experiments in ultra high vacuum (2×10^{-11} mbar) by using a variable temperature scanning tunneling microscope (STM) [73]. Ge was deposited by physical vapor deposition on Si(001) wafers with a 8° miscut angle towards the [110] direction at a growth temperature of 600 °C [66].

A series of STM snapshots at room temperature were recorded after each deposition, to image the morphology of the surface at every stage. We followed by the morphological evolution of the surface until the deposition of MLs of Ge. The results show that short zig-zag chains of Ge adatoms trigger the flow of double steps leading to the formation of metastable domains all aligned along the miscut direction [110]. Then the surface roughens abruptly due to the appearance of {105} facets on domain sidewalls perpendicular to the steps.

The faceted domains (ripples) are elongated toward the miscut direction and comprise a large number of D_B steps [73].

The average local slope of the surface toward [110] is 7.7°, as obtained by our STM measurements of the clean surface. Terraces 2.0 ± 0.2 nm wide with dimer bonds parallel to the step edge and D_B steps are observed. The rows on each terrace, consisting of a series of three dimers, are separated by 0.78 ± 0.01 nm.

At submonolayer Ge deposition the appearance of the $p(2 \times 2)$ reconstruction on the terraces, shown in Fig. 7(a), can be explained as resulting from an intermixing process [74] and implies the formation of Ge–Ge or Ge–Si dimers where Ge is the uppermost atoms [75] Furthermore, as reported by Lee et al. [76], and Kim et al. [77], rebonding at D_B step edges, which generates a 4% elongation of Si bonds, provides vacancy sites well suited for Ge incorporation. All these facts suggest that Ge is incorporated at the step-edge sites by replacing a Si atom to reduce the bond distortion energy of the (2×1) reconstruction. Such a process explains the uniformity of the terraces and the straightness of the step edge shown in Fig. 7(a).

The appearance of one-ML-high zig-zag chains, at 1 ML coverage, indicates that the growth proceeds by rearranging Ge atoms over the surface. Chains are composed by ad-dimers perpendicular to the dimers of the terraces (Fig. 7(b)). Their variable length suggests that they originate from an aggregation process of single ad-dimers as supported by previous works [76,78] on different configurations of Ge and Si ad-dimers on Si(001) surface. Nevertheless, in our case, chains have a preferential attachment site, as schematically illustrated in Fig. 8(b).

Taking the edge of the D_B step as a reference-point, the zig-zag chain is located two lattice parameters away from the step edge and consists of dimers located between dimers 1 and 2 of the terrace. Zig-zag chains allow the enlargement of the upper terrace and promote the shift of the D_B step edge, starting the step flow process. By increasing coverage, the flow of regular trains of D_B steps produces the disconnected domains seen in Fig. 9(b) over which new zig-zag chains form until, at 4 ML coverage, the domains develop reconstructed {105} facets (Fig. 9(c)).

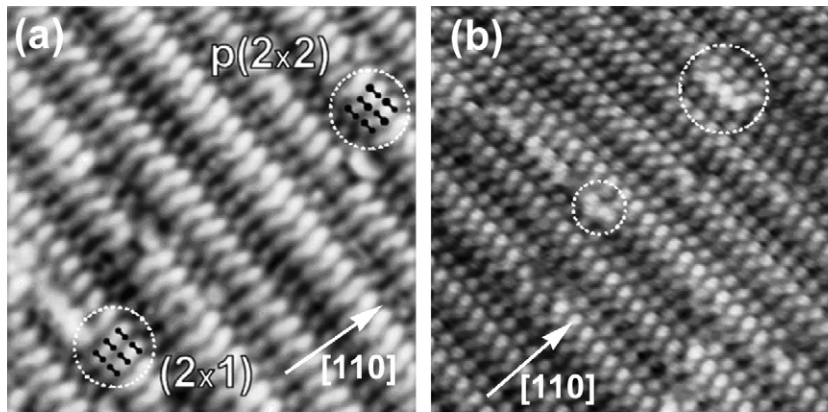

Fig. 7. STM filled-state images ($V_{bias} = -1.8$ V) of the 8° off Si(001) surface after deposition of 0.5 ML Ge (a); after 1 ML of Ge (b). Zig-zag chains deposited at 600 °C and dimer rows are highlighted. Scan areas are 15×15 nm^2.

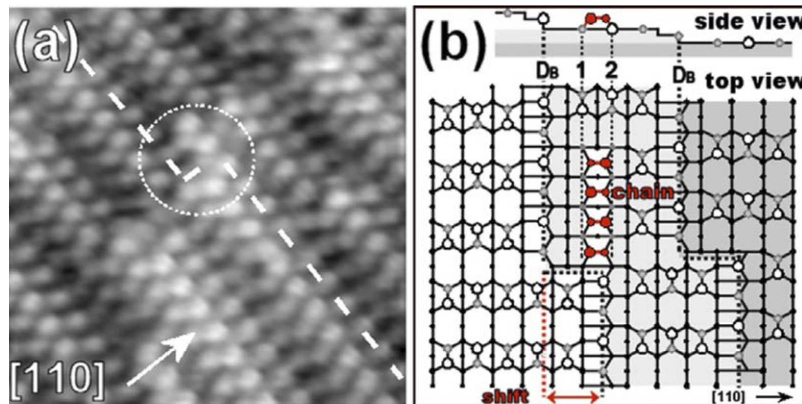

Fig. 8. (a) STM image 10×10 nm^2 of the vicinal Si(001) surface covered by 1 ML of Ge. The step edge shift by two lattice parameters and the zig-zag chain are highlighted (dashed ring). (b) Schematic representation (side view and top view) of the step edge shift and of dimers forming the zig-zag chain. Grey shades indicate different atomic planes.

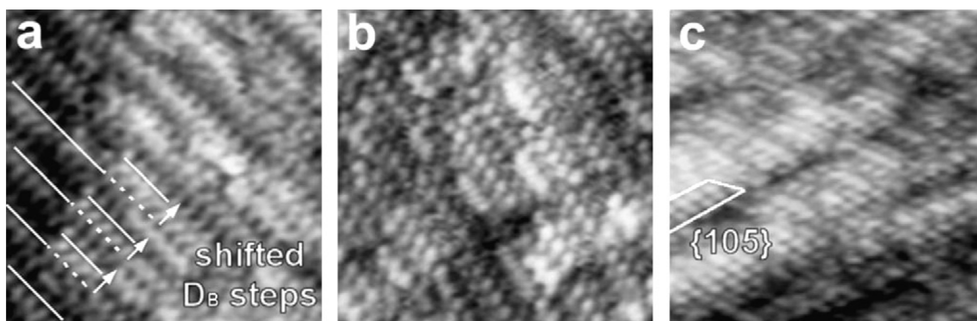

Fig. 9. STM images ($V_{bias} = -1.8$ V) of the vicinal 8° off Si(001) surface after different Ge deposition at 600 °C: (a) 2 ML; (b) 3 ML; (c) 4 ML of coverage. The propagation direction of the step edge; a single domain, a ripple and a {105} facet are evidenced. Scan areas are 15×15 nm^2.

The formation of ripples consisting of terraces and reconstructed facets has been modeled by P.D. Szkutnik et al. [73] demonstrating that on the vicinal 8° off Si(001) a surface with reconstructed ripples oriented along the [110] direction is finally obtained at 6 ML coverage. The average width of the ripples is about 40 nm.

It has been demonstrated by growing Ge on small lattice mismatched GeSi/Si multilayers, that Ge islands can be two dimensionally ordered by exploiting the periodic ripples due to step bunching [79]. Ripples provide preferential

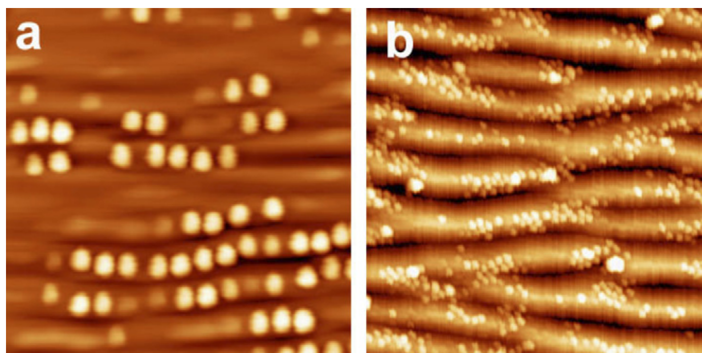

Fig. 10. 2×2 μm^2 AFM images of Ge deposited on 15 nm $Ge_{0.3}Si_{0.7}$/Si(118) at 600 °C with a ripple wavelength of 200 nm. (a) 8 ML Ge; (b) 0.5 ML Sb + 8 ML Ge. The miscut direction is horizontal in the plane view of the images.

nucleation sites on their ridges [5,79–81] allowing islands to macroscopically align along their direction. Substrate tilted at low angles (1–2°) along both [100] and [110] directions have been used by Zhu et al. [79], obtaining different ordering of the islands as a function of the substrate orientation.

We have recently demonstrated that the deposition of a layer of Ge–Si alloy on highly misoriented Si(001) substrates induces the formation of periodic undulations perpendicular to the step edges. These undulations form an array of alternate structures of valleys and hills that originate from step wandering and meandering, and their wavelength can be controlled by exploiting the molecular beam epitaxy (MBE) growth of small lattice mismatched Ge_xSi_{1-x}/Si(001). Their period and orientation are dependent on the alloy concentration and on the miscut angle [62].

Further Ge growth on such GeSi layers gives rise to islands which self-organize along the ripples, as they provide preferential nucleation sites for the islands because of the higher step density on their sides [4,82].

In Fig. 10 we show AFM images depicting the results of a two-step deposition process which consists of depositing Ge dots on a periodic unidirectional undulated $Ge_{0.3}Si_{0.7}$(118) template layer: the step meandering mechanism results in periodic sinusoidal-like topography with undulations perpendicular to the step edges. This results in an average wavelength of 200 nm. Ordering of Ge islands is achieved when the size of the islands matches the half wavelength of the patterned layer, so that the islands can be accommodated in the valleys or on the ridges. With no Sb deposition (Fig. 10(a)), large islands (100–130 nm in diameter) aligned on the ridges are observed. Lattice expansion on the hilltops and compression in the valleys can be ascribed as one of the causes of this preference, matching the 4.4% Ge lattice difference to the expanded Si.

The presence of 0.5 ML Sb causes Ge islands to be strongly reduced in size (Fig. 10(b)), but this dramatic reduction (∼50 nm diameter) (Fig. 10(b)) causes a scattering in their positioning.

Therefore, to obtain ordered smaller islands, we have to shrink proportionally their lateral size [83,84] and the ripple wavelength [80]. We have used Si(100) substrates 10° misoriented in the [110] direction, and a suitable composition x of the Ge_xSi_{1-x} alloy to obtain ripples of the desired wavelength [72]. A template layer of $Ge_{0.5}Si_{0.5}$ 3 nm thick with an average wavelength of 90 nm has been created by using solid-source molecular beam epitaxy equipment as detailed in [72]. A surfactant Sb layer has been deposited before the final Ge layer. The substrate temperature was maintained at $T < 400$ °C during Sb deposition (1/2 ML) to insure a sticking coefficient of 1. Fractional Sb coverage of 1/2 ML was alternately obtained by 1 ML Sb deposition at low T (400 °C) followed by partial desorption controlled by the temperature ramp to reach the growth temperature. Ge islands (deposited thickness ∼13 ML) have been grown on this template layer at 600 °C.

Atomic force microscopy (AFM) images of the samples were acquired after growth using a microscope operated in air. In Fig. 11 the effect of Sb coverage on the morphology and ordering of Ge islands is presented. We can see the islands aligning along the ripples, and forming close packed chains. The average island size is 35 nm. These islands are fully strained [83] and they present no visible facet, in contrast to hut islands exhibiting (105) facets that are obtained during Ge/Si(001) heteroepitaxy [18].

When the surfactant coverage is obtained by direct deposition (Fig. 11(a)–(c)) the Ge islands appear less ordered. We interpret this result as a consequence of the nucleation of Ge islands on Sb free areas which are distributed randomly below 1 ML coverage. The Ge nucleation sites are better organized by preferential desorption of Sb from

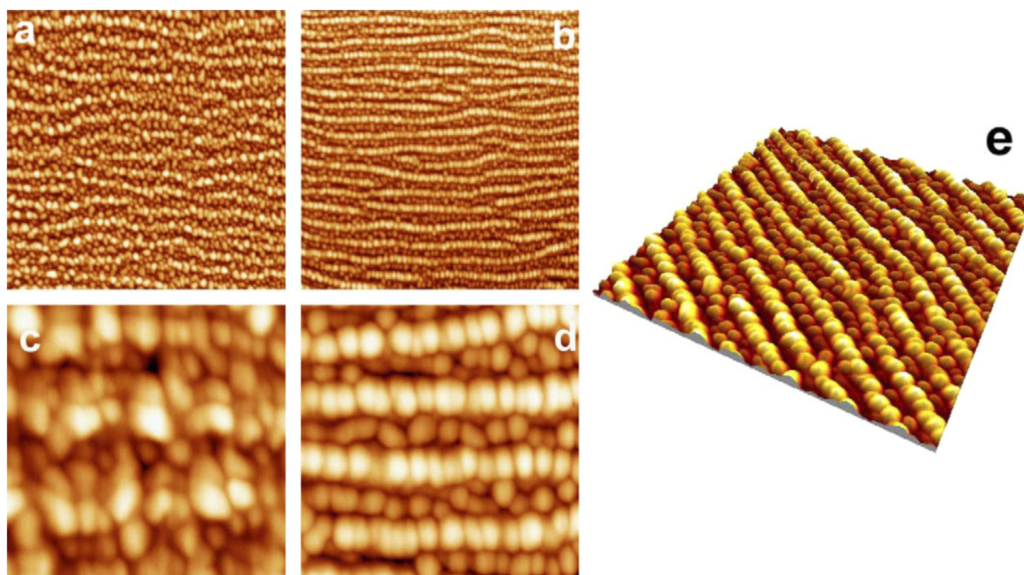

Fig. 11. (a), (b) 2×2 μm^2 AFM images of Ge deposited ∼13 ML on a template layer $Ge_{0.5}Si_{0.5}$ 3 nm thick with an average wavelength of 90 nm. The Sb coverage is 0.5. In (a) the 0.5 ML coverage was obtained by direct deposition, while in (b) it was obtained by controlled partial desorption from 1 ML. (c) and (d) Enlarged views (0.4×0.4 μm^2) of (a) and (b), respectively. The miscut direction is horizontal in the plane view images. (e) 3D view of (b) (1×1 μm^2).

the step edges. The sample in Fig. 11(b)–(d) was obtained by controlled partial desorption from 1 ML Sb, resulting in Sb coverage of ∼0.5. In these experimental conditions, islands align much better along the ripples and their shape is more homogeneous.

This experiment demonstrated that it is possible to control the nucleation site and organize ultrasmall Ge islands on a Si vicinal substrate by a combination of Sb surfactant-mediated growth of Ge and the creation of a suitable template layer by predeposition of a Ge–Si alloy.

7. Nucleation on patterned substrates

In spite of the good results shown in the previous paragraphs, the self-assembling process is still inadequate for the industrial mass production, because of the impossibility to predict the exact nucleation site of the QDs, and of their still large distribution in size. Moreover, the efficiency of the devices is largely dependent on the uniformity of the grown structures.

Very recent works [37–39], have shown that top-down (lithography) and bottom-up (self-assembly) processes can be usefully mixed, in order to place the dots at predetermined sites. The regular distance between the dots helps also to keep narrow their size distribution.

Among the many different possibilities for Ge/Si a new approach [34,50] based on recent studies [85], appears very promising. This method makes use of hole-patterned substrates to provide the desired dot nucleation sites. Holes in a Si substrate, covered by a controlled oxide layer, are produced by standard electron beam lithography, exposing the bare Si surface in selected regions where the Ge dots can nucleate and grow. It is well known, in fact, that Ge atoms do not attach to the oxide layer, so that only the Si clean surface allows the nucleation of QDs. A slight modification to this method makes use of a FIB (Focused Ion Beam) [33] to create holes, which should guarantee perfect cleanliness and controlled growth conditions.

Studies of the details of the nucleation process on substrates nanopatterned by STM have been undertaken by several groups [9,35]. While not viable for practical applications because of its intrinsic slowness, this method is very important to understand the details of the process and to localize the nucleation site, especially when the experiment is conducted in real time [35].

In the following we will illustrate the results recently obtained by STM and FIB patterning of Si substrates.

8. STM patterning

In this section a real time study of Ge deposition on Si(001) substrates patterned by using the tip of the scanning tunneling microscope is presented. The experimental observations provide insight into the WL formation in presence of a regular array of pits. The evolution of a specific hut from WL to pyramid is followed confirming the existence of a pre-pyramid stage, which evolves with the progressive insertion of {105} facets. Moreover, the results suggest that arrays of intentionally produced pits drive the nucleation process at selected sites [35]. A model based on step interaction is applied to estimate the influence of a pit on the pre-pyramid.

The Si(001) substrate (p type, $\rho = 0.1$–$0.5\ \Omega\,\text{cm}$), was annealed by dc heating at 1250 °C in ultra-high-vacuum. A clean (2×1) reconstructed surface was obtained. Then, at 500 °C, the surface was nanopatterned by using STM lithography. At selected positions, with the z-feedback switched-off, pits were elaborated by approaching the STM tip to the surface. The array was re-imaged during the next scan. Pits have diameters ranging from 8 to 15 nm and depths of 1–2 ML and the distance between them is 60 ± 5 nm. Before deposition, the stability of the array was assessed by a long annealing process (30 min). On the nanopatterned surface, the growth of Ge by physical vapor deposition was recorded in real-time by STM. In this kind of experiments a tip shadowing effect [7] occurs causing a lower growth rate in the scanned area. The Ge coverage is estimated from the increasing area of terraces between two successive images during the layer-by-layer growth. A Ge flux of $(2.6 \pm 0.3) \times 10^{-3}$ ML/s was evaluated and kept constant.

Fig. 12 shows a nanopatterned Si(001) surface after annealing at 500 °C for 3 hours, confirming the stability of the holes with temperature. Also a profile of a hole is shown in the inset: the hole is about two layers deep and 12.5 nm wide.

Figs. 13(a)–(d) display four images extracted from an STM movie of Ge growth. At the beginning, a step flow process occurs meaning that the WL forms on the step edge enlarging the terraces. It appears that the WL encloses the pits that are not filled up by Ge, and increases the surface roughness. The analysis of this sequence is represented in Fig. 13(e) by the evolution of the pits' depth and diameter changes as a function of Ge coverage, θ. To understand the growth mechanism of Ge atoms with respect to the pits, the sign of the 'depth rate' (DR), defined as the slope of the fitted pit depth, is analyzed. In the present case the fit provides a value of $\text{DR} = 0.09 \pm 0.01$ nm/ML indicating that a

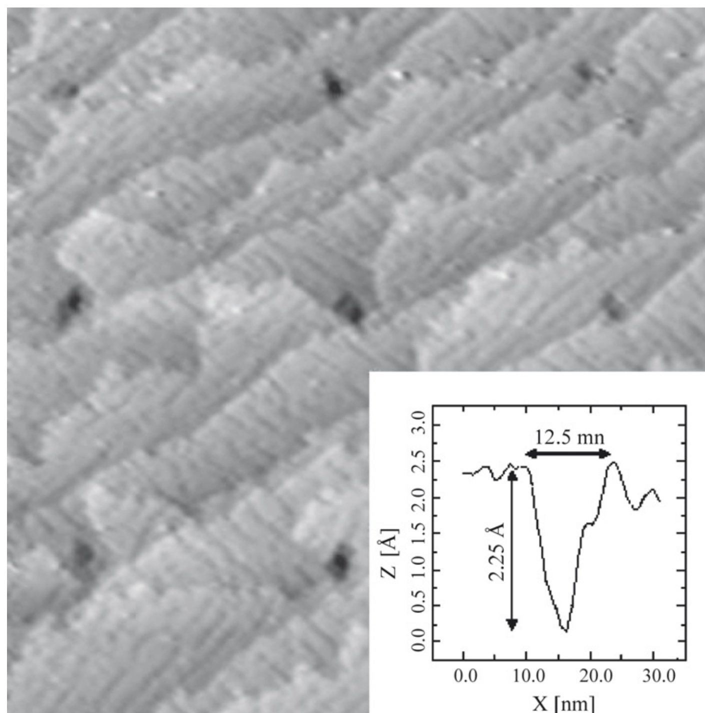

Fig. 12. STM image $(170 \times 170 \times 2)\ \text{nm}^3$ of an array of holes elaborated with the STM tip and annealed at 500 °C for three hours. In the inset is reported the line profile of the hole in the centre of the image.

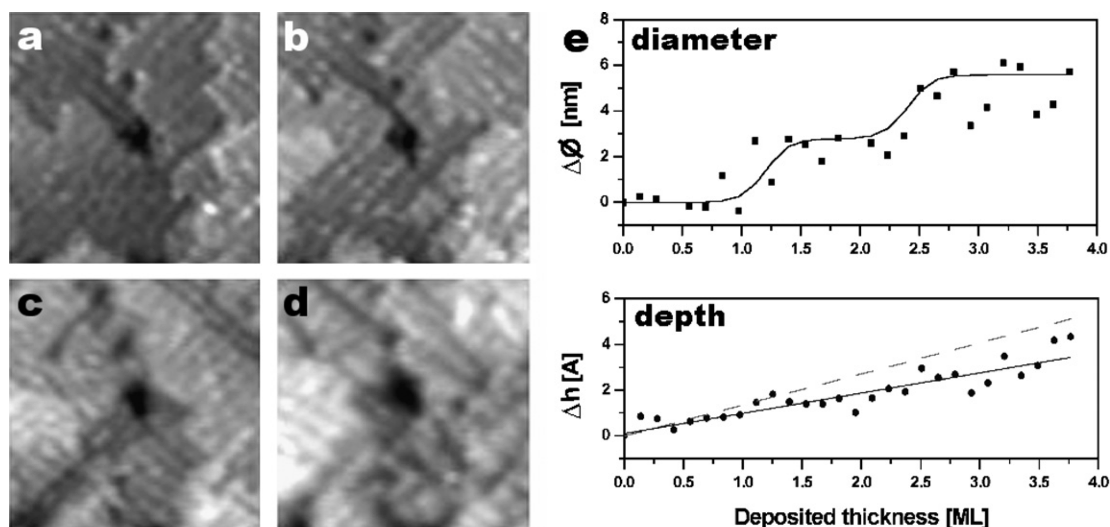

Fig. 13. Formation in real time of the WL on a nanostructured Si(001) surface; zoom on a hole. (a)–(d) STM images $(50 \times 50 \times 0.5)$ nm^3 extracted from the movie of Ge deposition at 773 K at a coverage of: (a) 0.89 ML; (b) 0.99 ML; (c) 1.24 ML; (d) 1.48 ML; (e) Relative evolution of the pit morphology as a function of the deposited thickness ($\Delta\varnothing$ the diameter and Δh the depth). The experimental data correspond to full dots, the respective fits to full lines. The dashed line shows the thickness of the deposited Ge layer.

few Ge atoms go inside the pit. Therefore the data analysis confirms that Ge atoms do not completely fill the pit. The pits' diameter versus deposited thickness plot in Fig. 13(e) provides information about the localization of Ge atoms. A constant diameter means that the WL ends at the border of the pit. Here, the diameter increases, jumping every 1.15 ML of Ge coverage. A good fit to the experimental data is obtained using a step function with 2.8 nm jumps which gives an equilibrium distance of 1.4 ± 0.3 nm between the step edges of two adjacent layers (Fig. 14). This distance corresponds to the space needed to host a $p(2 \times 2)$ or $c(4 \times 2)$ reconstructed unit cell. So the new growing layers form an angle of $5.5 \pm 0.2°$ with the surface close to 6°, the critical angle reported by Sutter et al. [86].

The 2D–3D transition takes place between 3 and 4 ML of Ge coverage. The real-time growth of a Ge hut cluster (circled in Fig. 15(a)) is shown in Fig. 15(a)–(e).

In this sequence, two different stages of growth can be identified: the first corresponds to the formation of a pre-pyramid (at $\theta = 3.23$ ML, Fig. 15(a)), while the second one to a pyramidal hut (at $\theta = 3.79$ ML, Fig. 15(e)). Close to the bottom and to the right corner of the pyramid it is possible to identify two holes in the surface, giving reason for the location of the nucleation [35]. Generally is possible to identify a hole as seeding point for each of the nucleated islands. This is especially evident in the island on the extreme left of the images, which has the bottom left corner on the edge of a hole.

The evolution of the 3D line profile (Fig. 16(a)) and volume (Fig. 16(b)) of the 'circled' cluster is plotted as a function of coverage. In Fig. 16(a), the profiles between 2.11 and 2.95 ML illustrate the WL formation. At $\theta =$ 3.23 ML, a new structure which grows laterally is distinguishable (arrowed in Fig. 16(a) and circled in Fig. 15(a)) and corresponds to a two-layer-high platelet. Then, successive small layers form upon it, reaching a height of 0.8 nm.

The corresponding line profile shows a very clear transition to the characteristic shape of a hut cluster. At $\theta =$ 3.79 ML, a complete square base pyramid is observed which grows by developing its four $\{105\}$ facets [18,87]. This is apparent on the line profiles from 3.79 to 4.21 ML: these have triangular shapes with constant slope but height and base progressively increasing. The height-to-width ratio varies between 0.015 and 0.03, in good agreement with that measured by Vailionis et al. [19] and reaches 0.1, when the transition (dashed area in Fig. 16(a)) to a pyramid is completed.

Quantitative information on the growth mechanism can be obtained from the volume of the hut as a function of θ. The volumes measured on a selected and fixed area have been analyzed from $\theta = 0$ ML up to the appearance of a fourfold pyramid at $\theta = 4.21$ ML, and three regimes (Fig. 16(b)) have been identified, on the basis of STM images, as WL, 2D–3D transition and pyramid growth. Interestingly, the larger rate of 1670 nm^3/ML during the development of the pyramid indicates that more atoms than those deposited on the selected area are required. As the Ge flux is

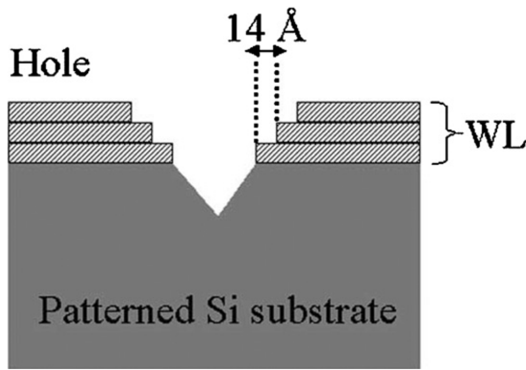

Fig. 14. Schematic evolution of a pit during Ge deposition.

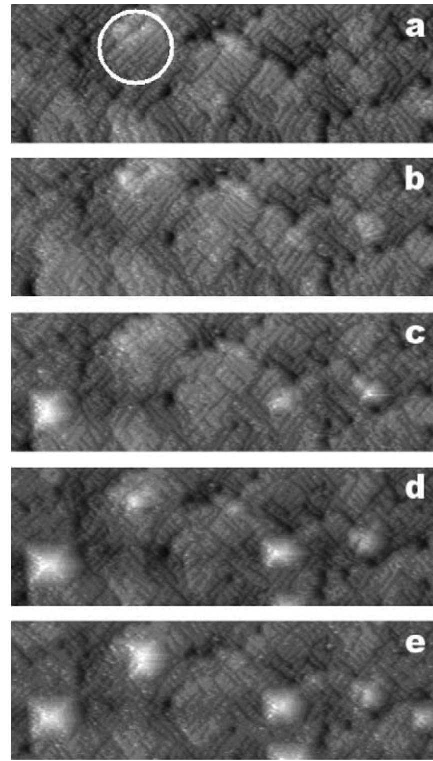

Fig. 15. Formation in real time of the pyramid on a nanostructured Si(001) surface. (a)–(g) STM images $(250 \times 80 \times 3)$ nm^3 extracted from the movie of Ge deposition at 773 K at a coverage of: (a) 3.23 ML; (b) 3.37 ML; (c) 3.51 ML; (d) 3.65 ML; (e) 3.79 ML.

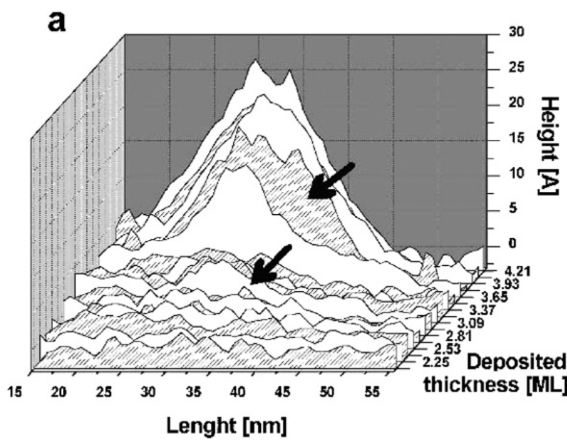

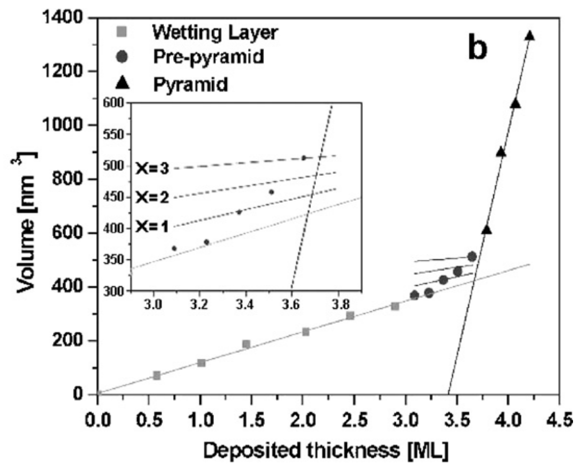

Fig. 16. (a) Evolution of the profile of the hut cluster (marked in Fig. 15(a) by a circle) as a function of the deposited thickness. The two arrows indicated the first step of the pre-pyramid formation and the complete formation of a pyramid, respectively; (b) Evolution of the volume of the same hut cluster as a function of the deposited thickness. The experimental data are represented by three symbols for each type of the hut cluster identified thanks to STM images (squared shape for WL, rounded shape for pre-pyramid and triangular shape for pyramid); the lines represent the fit for each regime.

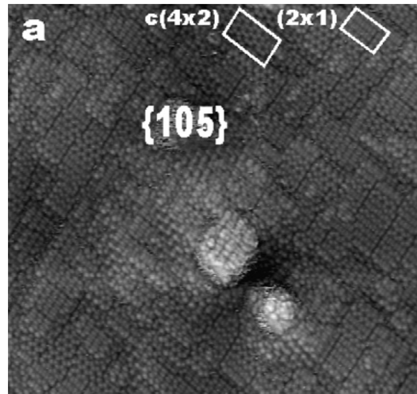

Fig. 17. STM images of different hut clusters on Si(001) surface. (a) STM image $(100 \times 100 \times 3)$ nm^3 of a pre-pyramid where one of the {105} facets and two different surface reconstructions, namely the (2×1) and the $c(4 \times 2)$ are evidenced.

constant and no depletion region is observed around the hut, a germination process has to take place. Specifically, Ge atoms diffuse towards the pyramid from a collection (Voronoi) area larger than that selected. This area, assumed to be a square, has a side of 95 nm as evaluated from the ratio of the slopes of the first and third regimes. Hence, a density of the 3D clusters of 1.1×10^{10} cm^{-2} is calculated comparable with 3×10^{10} cm^{-2} obtained from STM images.

At $\theta = 3.66$ ML, the two fits cross over indicating that the material accumulated during the WL growth is enough to generate a hut cluster by a rearrangement of its initial structure [19,8]. We assume that the growth of a pre-pyramid starts when the volume deviates from the linear behavior in the second regime. Between 3 and 3.79 ML, a transition region occurs characterized in Fig. 17 by the coexistence of (2×1), $c(4 \times 2)$ reconstructed domains and {105} incomplete facets.

According to the STM image in Fig. 16(b) [35], these experimental evidences suggest that a first layer forms on the WL corresponding to the base of the future pyramid. Then, by increasing θ, new layers grow on top of each other. These overlapping layers extend until to form an energetically favored {105} facet [88]. The coalescence of disconnected {105} domains leads to the formation of a pyramid facet and eventually to a hut cluster.

The volume of the pre-pyramid as a function of coverage can be expressed by:

$$V(\theta) = \frac{X}{4} \times V_P + \left(1 - \frac{X}{4}\right) \times V_{\mathrm{WL}}(\theta) \tag{8.1}$$

where V_{WL} is the volume of the overlapping layers, equal to that of the WL, and $0 \leqslant X \leqslant 4$ is the fraction of {105} facet. V_P,[1] equal to 542 nm^3, is defined as the volume of the pyramid just after the 2D–3D transition. The volumes are calculated from Eq. (8.1) for different values of X and for θ corresponding to the coverage of the experimental data. Good agreement between calculated and experimental volumes is found for integer values of X. This means that, during the transition, the system evolves as a pre-pyramid composed progressively by one ($X = 1$), two ($X = 2$), or three ($X = 3$) complete {105} facets. Under the above hypotheses, the 2D–3D transition can be described as a successive insertion of complete {105} facets. The presence of a critical nucleus with a stepped shape which evolves up to the appearance of {105} facets is also suggested by Sutter and Lagally [89], but they did not specify if all facets appear simultaneously. Our volume data can also be reproduced by using the model of Tersoff et al. [3] considering a constant base of 14 nm and a base's angle continuously increasing up to 11°. However, this model does not explain the presence of partial {105} facets.

Considering the lateral arrangement, it is remarkable that a pre-pyramid always nucleates around a pit. To evaluate the relaxation energy originating from elastic interactions between islands and pits, our system is described [35] by a

[1] V_P is estimated from Eq. (8.1) assuming that at 3.65 ML, where the volume is 512 nm^3, the pre-pyramid has three reconstructed and a single unreconstructed {105} facet.

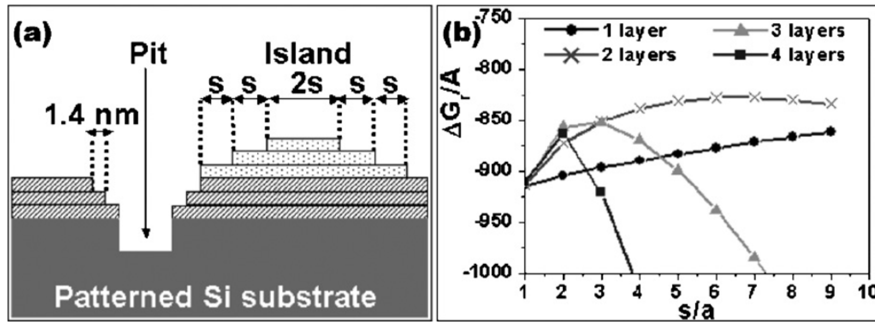

Fig. 18. Calculated relaxation energy for a pre-pyramid near a pit using the one-dimensional elastic interaction model described by Eq. (8.2) of the text. (a) Cross-sectional schematic representation of a pit and a three-layer high island considered for the calculation. (b) Evolution of the normalized relaxation energy, $\Delta G_r/A$ as a function of the step width s for an island one- to four-layers high. $A = C\sigma^2 h^2$, where σ is the bulk stress of the epilayer, h is the step height and $C = (1-\nu)/(2\pi\mu)$ is the misfit stress where μ is the shear modulus and ν is the Poisson's ratio.

stepped island (with steps of equal spacing s) adjacent to a four-layer-deep square pit. The model takes into account repulsive or attractive monopole interactions between the steps [90,47]:

$$\Delta G_r = A \sum_{i \neq j} \operatorname{sign}(i) \operatorname{sign}(j)(x_i - x_j) \ln\left(\frac{x_i - x_j}{a}\right) \tag{8.2}$$

where A is a constant, sign $= \pm 1$ counts the attractive (+) or repulsive (−) interaction between two steps with the same or opposite orientation, respectively, $x_i - x_j$ is the distance between the steps i and j and a is a cutoff length of the order of the lattice parameter of Ge. By plotting $\Delta G_r/A$ as a function of s/a for a different number of layers forming the island, Szkutnik et al. [35] have demonstrated that for a one-layer high island, growth is unlikely, while two-layer-high pre-pyramids have increasing relaxation magnitude for $s/a > 8$ and thus high probability to grow. A width of 16 nm and an aspect ratio of 0.017 result from the calculation for a square-base pre-pyramid, consistent with the experiment. With the same reasoning, by increasing the height from two to four layers, smaller size pre-pyramids can nucleate near the pit. In general, the localization of pre-pyramids is driven by the local chemical potential which contains two contributions. The relaxation of the strain energy selects small pits as nucleation sites [47] (near the pit) while the curvature term becomes important for large pits [91,92].

9. FIB patterning

Focused Ion Beam (FIB) technology is becoming an extremely important tool in semiconductor manufacturing and its applications have gone far beyond Integrated Circuits photomask repair (which was the original driving force for developing FIB systems). Microstructure fabrication is the latest outgrowth of FIB milling applications. Another emerging field of application is the production, at the nanoscale, of 3D nanostructure arrays, using performances of high resolution FIB instrument [93]. FIB nanopatterning is a unique technique since it has the capability of high-resolution direct writing of the Si substrate. It exploits the precise, computer controlled, maskless, sputter etching afforded by a beam of 15–30 keV Ga^+ ions focused to a 10 nm spot to fabricate features in semiconductor wafers. The beam of ions emitted by the liquid metal source is apertured and focused in an ion-optical column which, depending on the design, can provide a focal spot as small as ∼10 nm. A significant advantage of FIB is that it is completely maskless process and no photolithography wet chemistry or other processing is required.

By using FIB patterned surfaces, it has been recently shown the possibility to control the nucleation of large arrays of Ge quantum dots on Si(001) and SiO_2/Si(001) substrates [94,95]. M. Kammler et al. [96] have affected the nucleation by using the surfactant effect of the implanted Ga^+ ions and achieved a good control of the position of Ge QDs. Our group instead, aiming to study the Ge nucleation on clean patterned Si(001) surfaces, has developed a restoring procedure to desorb the Ga^+ contamination from the surface. We have relied mostly on the perturbation of the flat surface generated by the FIB holes, in order to generate preferential nucleation sites for our quantum dots.

FIB patterned samples were produced by FEI Company. Their Dual Beam System FIB uses a liquid metal ion source to generate a Ga^+ ion beam ($I \approx pA$, $V = 5$–25 keV) at normal incidence and at a very low distance from the sample surface.

Two kinds of patterned surfaces were studied: a bare Si(001) surface and a 5 nm thick SiO_2 layer grown on Si(001) substrate. In the first case, we followed, in real time, the growth of Ge nanostructures using a Scanning Tunnelling Microscope (STM). In the second case, we used an Atomic Force Microscope (AFM) to study the distribution of Ge droplets generated, after thermal annealing, on an amorphous layer. Our experimental results throw light on several issues such as substrate nanostructuring, 3D islands formation, arrangement, lateral ordering and size uniformity of QDs.

9.1. Si(001) substrates

After FIB patterning, the Si(001) samples undertook a cleaning treatment in an ultrasonic bath of diluted HCl (1:10) followed by a rapid thermal annealing at 1300 K for 1 min in N_2 atmosphere to remove Ga atoms embedded in the Si matrix. The measured concentration of Ga after this treatment was below 4×10^{16} at cm^{-3}. Then, a new annealing in Ultra High Vacuum at 873 K for 30 minutes was carried out in order to get rid of residual contaminations. Images of the array of holes in UHV have been obtained by STM immediately after this treatment as a final check (Fig. 19(a)). Two different arrays of pits with depth of 30 nm, diameter of 150 nm and a periodicity of 780 ± 30 and 500 ± 30 nm respectively have been produced on the Si(001) bare substrates. On these surfaces we have followed in real-time the Ge growth at a temperature of 873 K.

As displayed in Fig. 19 at 2.5 ML, the nucleation starts nearby a hole and develops into a Ge island covering the entire pit. This occurs in most cases, producing a nicely ordered pattern at 8 ML coverage.

In Fig. 20, Si(001) surfaces with two different pitches of 780 and 500 nm are visualized after 8 ML of Ge coverage. The increased islands density in the sample with smaller pitch is evident. In particular in the case of the large pattern (Fig. 20(a)), the island density is measured to be 1.9×10^8 islands·cm^{-2}, close to the hole density 1.7×10^8 holes·cm^{-2}, while, for the second pattern (Fig. 20(b)) with a density of holes of 4×10^8 holes·cm^{-2}, the island density is about 3.4×10^8 cm^{-2}. It is apparent that the island pattern follows strictly the pit pattern. In order to identify the nucleation site in Fig. 21(b) we have indicated the corresponding position of pyramids and domes with respect to that of visible and hidden pits. All pyramids (except one) start nucleating nearby a pit and then grow over the pit. We conclude that nucleation starts preferentially at the border of pits. Subsequently islands, increasing their size, evolve covering the underlying pits.

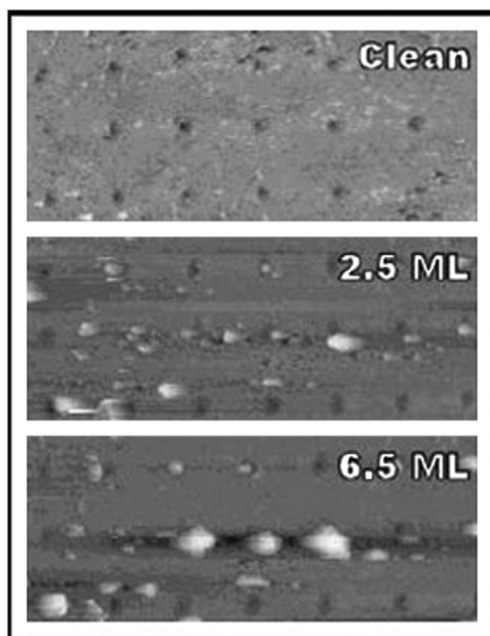

Fig. 19. Sequence of STM images (4.5 μm × 2.5 μm) recorded in real time during Ge deposition at 873 K on a FIB patterned Si(001) substrate with a 780 nm pitch, starting from the clean surface up to 6.5 ML coverage.

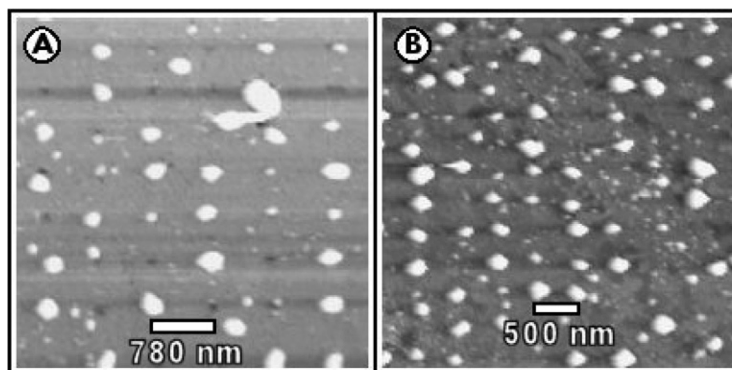

Fig. 20. STM images (5 μm × 5 μm) for 8 ML deposition of Ge at 873 K on Si(001) patterned surface with pitch values of (a) 780 nm and (b) 500 nm.

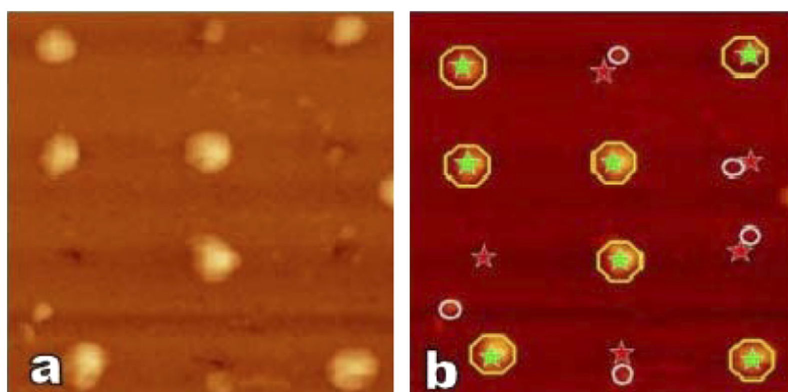

Fig. 21. (a) STM (2.5 μm × 2.5 μm) microscopic image of the island morphology and position on a FIB Si(100) patterned surface with 780 nm pitch. (b) Identification of the image features. Red stars: empty pits. Green stars: overgrown pits. Circles: pyramid islands. Octagons: dome islands. Stars: FIB pits. Open circles: Ge islands.

After 20 ML Ge deposition (Fig. 22(a)) the difference in ordering between non-patterned (Fig. 22(b)) and patterned area (Fig. 22(c)) is evident. The density of the islands on the patterned region is estimated to 2.1×10^8 cm^{-2}. Moreover, the different degree of ordering outside and inside the patterned area is evidenced by the Fast Fourier Transform (FFT) made on these two selected regions. As a result the FFT analysis allows measuring a well-defined periodicity for Ge islands equal to 790 ± 50 nm on the patterned region (Fig. 22(c)), while, outside, the FFT does not show any spot (Fig. 22(b)), demonstrating the absence of lateral ordering where arrays of pits are not present. The statistical analysis of the diameters of islands nucleated on patterned and non-patterned areas offers another interesting issue. Regarding the size distribution of islands (Fig. 22(d)), a Gaussian fit yields a mean diameter of 280 nm for islands grown on the unpatterned surface, whereas for the islands grown on the patterned surface, a bimodal distribution with two peaks at 80 and 285 nm appears.

To identify the origin of these two different nanostructures, a further analysis of the islands grown on the patterned surface, by discriminating islands nucleated in correspondence or between the holes, has been performed. We found a single peak at 280 nm for islands corresponding to holes, and we note that the same value was previously obtained for islands randomly nucleated on the unpatterned region. We conclude that the patterning does not affect the growth mode, but strongly affects the lateral ordering of islands. Moreover, as displayed by the size distribution Fig. 22(d), we show that the double peak on the patterned surface results from the nucleation of islands in between the holes. The peak at 80 nm corresponds to the formation of a further generation of islands drawing the residual Ge available on the substrate [97]. This effect can be reduced by reducing the pitch of the array to that of the collection area for the formation of a pyramid [34], since the mean free path of Ge atoms is limited [98].

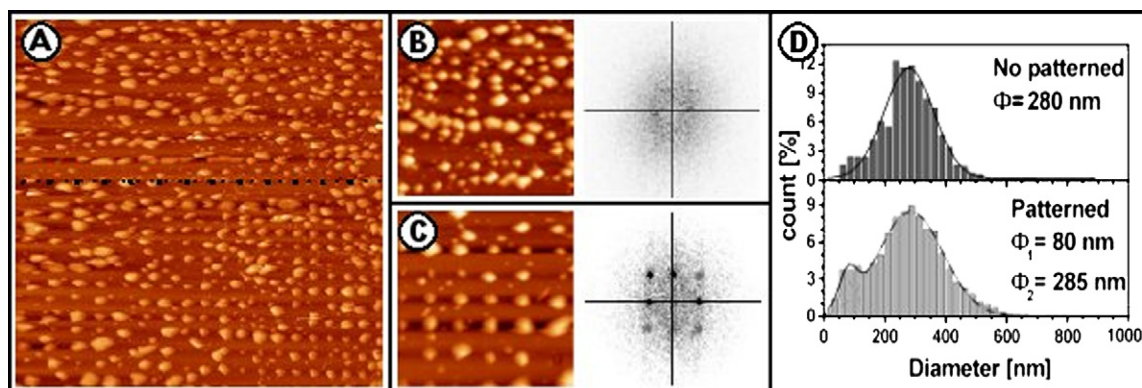

Fig. 22. (a) STM image (18 µm × 18 µm) after 20 ML of Ge deposited at 873 K on a FIB patterned region of a Si(001) surface with a pitch of 780 nm. The dash line separates the patterned from the unpatterned area. (b) Zoom (5 µm × 5 µm) on the unpatterned area and the Fast Fourier transforms of the images, (c) zoom (5 µm × 5 µm) on the patterned area and the Fast Fourier transforms of the images. (d) Diameter distributions of the islands for the two regions.

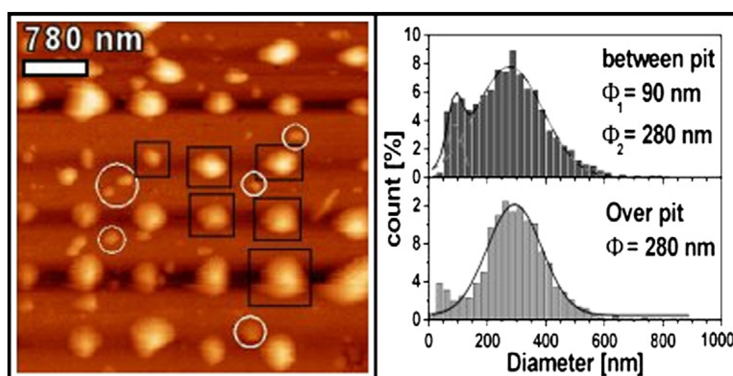

Fig. 23. STM image (5 µm × 5 µm) after 20 ML of Ge deposited at 873 K on a FIB patterned Si(001) surface with a pitch of 780 nm and the corresponding diameter distributions of the islands. The circles highlight the islands grown between pits and squares those grown over a pit.

Recently Karmous et al. [99] have analysed island growth in similar conditions by MBE at two different temperatures, 823 and 973 K. Their results suggest two different mechanisms of island formation: inside the FIB holes at low temperature (823 K) and on edges of the holes at high temperature (973 K). They discuss the influence of holes array on the local chemical potential at the surface. The difference of the chemical potential of a patterned surface as compared to a planar surface can be expressed by [100], $\Delta\mu = \Omega\gamma k(x, y) + \Omega E_{\mathrm{el}}(x, y)$, where the first term $= \Omega\gamma k(x, y)$ describes the change of the surface energy γ with the surface curvature $k(x, y)$ and the second term $\Omega E_{\mathrm{el}}(x, y)$, describes the change of the local strain energy $E_{\mathrm{el}}(x, y)$, induced by the holes. Their findings match very well our results shown in Figs. 21 and 23: at high temperature (973 K), Ge islands nucleate mainly on the sides of the holes, because the enthalpy of formation is lowered on a curved surface, where the lattice can expand to accommodate the larger Ge atoms. However, for lower substrate temperatures it has been demonstrated that Ge islands nucleate at the centre of the holes, because the reduced mobility favours the attachment on regions where more steps and defects are present.

9.2. Flat SiO_2/Si(001) substrates

To evaluate the effect of patterning on SiO_2 surfaces, we have studied Ge nucleation on SiO_2 substrates without patterning. It is known that Ge does not stick on SiO_2, and Ge droplets are formed instead. This effect has been exploited in order to obtain, at the same time, smaller Ge dots and electrical insulation, in view to the application of these dots as memory cells.

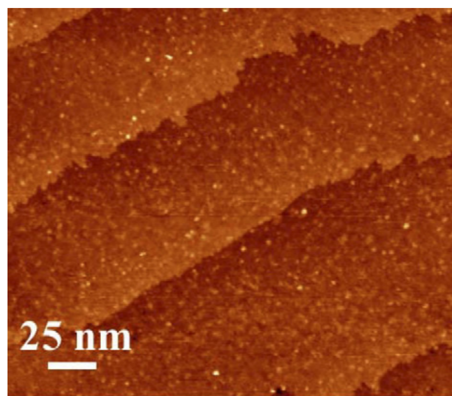

Fig. 24. STM image of a clean SiO_2/Si(100) surface.

The mechanism of Ge islanding on a SiO_2 substrate is different from that on Si because it is basically driven by surface diffusion and equilibrium surface morphology [101]. In this case a Volmer–Weber growth of Ge islands is observed without the formation of a wetting layer, thus allowing a higher dots density [102–106].

Clean SiO_2 surfaces were prepared by rapid thermal annealing at 1223 K of Si(001) substrates in ultrahigh vacuum and Ge was evaporated using an electron gun with a rate of 0.1 nm/min at pressure of 1×10^{-10} Torr during deposition. Four MLs of Ge were deposited at room temperature, then the sample was annealed in-situ at 773 K for 30 min. In this way we obtained crystalline Ge dots with average size of (5 ± 1) nm and very high density of about 3×10^{12} cm^{-2}. The surface was examined in-situ at room temperature by STM. Ge dots appeared almost flat with the onset of (001) and (113) faceting and were characterized by a low aspect ratio. Such a morphology is attributed to the thermodynamic equilibrium shape of Ge. From the I–V curves we measured an energy gap of about 1.8 eV that is much wider than that of bulk Ge, thus suggesting the occurrence of quantum confinement.

The STM image of the clean SiO_2 surface used as template for Ge deposition, shown in Fig. 24, nicely mimics the shape of the Si(001) surface underneath, i.e. a perfect sequence of terraces 70 nm wide and of monoatomic steps. On terraces we observed small isolated brighter protrusions, with a density of about 1×10^{13} cm^{-2}, forming a rough substrate of 0.06 nm Root Mean Square (RMS) roughness.

Fig. 25(a) shows the STM image after 4 ML deposition of Ge at room temperature. At this stage, full coverage of the SiO_2 surface has been achieved and randomly distributed, strictly interconnected Ge amorphous clusters have been formed with a RMS roughness of 0.27 nm and a density of about 4×10^{12} cm^{-2}. Subsequent heating at 500 °C changed the surface morphology giving rise to individually separated Ge dots with a density of $\sim 3 \times 10^{12}$ cm^{-2} (Fig. 25(b)). Such a value is approximately the same as that reported for Ge dots grown on SiO_2/Si(111) surfaces kept at 670 °C [104], but higher than that found for Ge dots deposited on clean and/or lithographically patterned Si surfaces [4,7,35]. The Ge dots average lateral size is (5 ± 1) nm. Statistical analysis, carried out on about one hundred islands, gives an aspect ratio, η, of (0.17 ± 0.04), a value lower than all those reported in literature for similar and higher coverage [102,105,107]. Besides, the most striking aspect reported is the hemispherical-like shape characterising the dots [104–106].

To investigate this point, we supplemented the STM image of the Ge dots with the image analysis following the procedure described by Rastelli and von Känel in the case of Ge deposited on clean Si(001) surfaces [108]. This analysis provides the Miller indices of the facets by computing the two-dimensional histogram of the surface gradient of the function $f(x, y)$, i.e. the height of each pixel forming the STM image. In Fig. 26(a) we show a typical two-dimensional histogram of the opposite of the gradient $[-\nabla f(x, y)]$ carried out on the whole STM image of the sample (shown in Fig. 25(c)). This histogram has circular symmetry around the centre that is made of all the points in the STM image having 'zero slope'. This result evidences a large flat area on top of each dot parallel to the (001) planes of the Si substrate. This top facet has been proven to be (001) oriented. Indeed, RHEED patterns (not shown) of thicker Ge deposits on SiO_2/Si template layer exhibit the typical 2×1 reconstruction of (001) Ge facets and clearly prove that Ge dots top facet has (001) orientation parallel to the underlying substrate. The absence of isolated spots (Fig. 25(c)) can be related to the random orientation of the dots induced by the heterogeneous nucleation on the SiO_2 surface and by the absence of any epitaxy onto the bare Si substrate. Moreover, the broadening of the central area suggests the

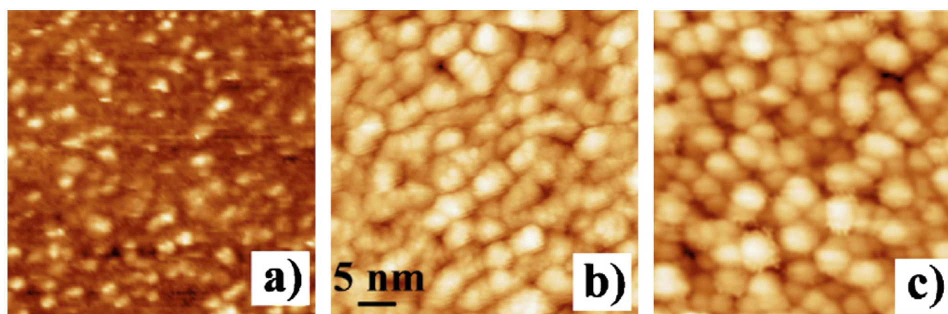

Fig. 25. (a) STM image of the SiO_2 substrate. $V_{sample} = -3.0$ V, $I = 0.5$ nA; (b) STM image of 4 MLs of Ge deposited on a SiO_2/Si(001) surface kept at room temperature. $V_{sample} = 2.0$ V, $I = 1.0$ nA; (c) STM image of the sample shown in the panel (b) after annealing at 500 °C for 30 min. $V_{sample} = 3.0$ V, $I = 0.5$ nA.

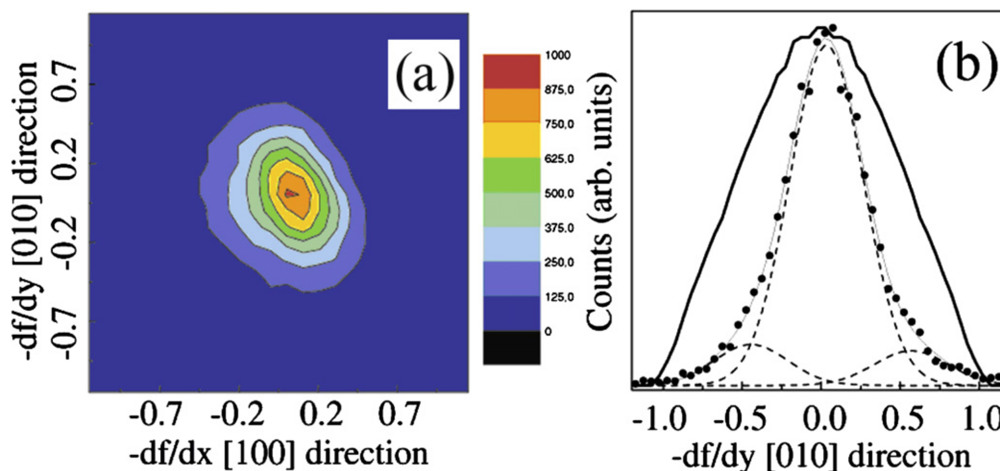

Fig. 26. (a) 2D dimensional histogram of the opposite of the gradient carried out on several STM images of the sample shown in Fig. 25(a); (b) Section of the histogram ($-\mathrm{d}f/\mathrm{d}x = 0$) shown in the left panel (full dots) compared to the same section of a histogram computed for a spherical cap with aspect ratio 0.17 (bold solid line). The dashed curves are the components corresponding to the zero slope and to the {113} facets.

presence of facets on the side of the dots slightly tilted with respect to the (001) plane. In order to check if this result is compatible with the hemispherical shape of the dots we generated the histograms of $[-\nabla f(x, y)]$ for a spherical cap-shaped dot with different aspect ratios (η) ranging from 0.5 to 0.1. By varying η, the simulated curve is slightly affected, thus suggesting that its width is mainly determined by the spherical cap shape. In Fig. 26(b), we compare the same section of the experimental (dotted line) and simulated (bold solid line) histograms taking the measured $\eta = 0.17$. No accordance is found. The best fit to the experimental line shape is obtained using three Gaussians distributions (dashed lines), one centred at zero slope and the other two at angles around 26°. This result suggests that the Ge dots are almost flat with side facets close to the {113} planes.

This is also confirmed by the RHEED pattern (not shown) of a thicker Ge deposit on 7 nm SiO_2/Si(001) showing facets forming an angle of $27° \pm 2°$ which is associated to the {113} planes. As predicted by nucleation and growth theory, Ge dots' morphological evolution during thermal annealing (on amorphous substrate) is dictated by the thermodynamic equilibrium shape of Ge. We can then conclude that (001) and (113) represent minimum surface energy facets.

9.3. Patterned SiO_2/Si(001) substrates

Dense holes arrays (4×10^{10} holes cm^{-2}) were produced by FIB on oxidized Si (Fig. 27). In this case, a double procedure of oxidation and chemical etching has been undertaken, in order to develop a 5 nm clean SiO_2 layer presenting a patterned surface [107,99]. The FIB patterned substrates were chemically cleaned in an HCl:H_2O solution followed

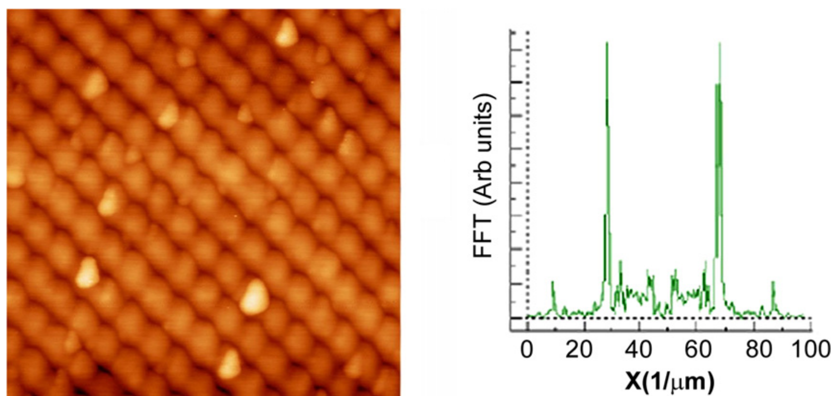

Fig. 27. AFM (0.6 μm × 0.6 μm) image of a SiO_2/Si(100) FIB nanopatterned surface (left). The Fast Fourier Transform of the AFM image has been used to determine the average distance between the holes $\ell = (51 \pm 1)$ nm (right). The average depth of the holes is 4 nm.

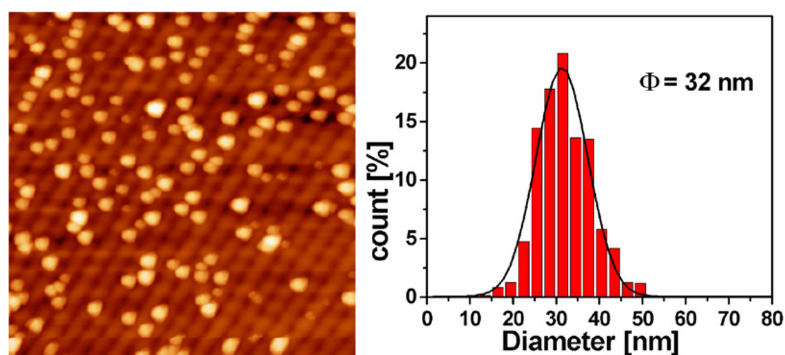

Fig. 28. STM image (1 μm × 1 μm) after 5.2 ML of Ge deposited at 873 K on a FIB patterned $SiO_2/Si(001)$ surface with a pitch of 50 nm. At the right, the size distribution.

by annealing and another HCl bath to remove the Ga contamination induced by the FIB process. The efficiency of this restorative process in removing the Ga atoms was checked using secondary ion mass spectrometry (SIMS) measurements (the Ga concentration measured was below the detection limit of SIMS, $10^{16}/cm^2$). The samples were then chemically cleaned and oxidized before being loaded into the growth chamber.

A first experiment consists in depositing 5.2 ML of Ge at 873 K. The surface (Fig. 28(a)) displays randomly nucleated islands on the patterned SiO_2 surface [109]. Some islands seem to nucleate inside the holes, others nearby. Some regions are free of islands. Nevertheless, a mean diameter of 32 nm is extracted from the size distribution with a FWHM $\sigma = 10$ nm. At this growth temperature, the surface topography does not play a crucial role and does not affect the lateral ordering.

In a second experiment, Ge was deposited at room temperature to form an amorphous layer that is subsequently annealed at high temperature (773 K) for 20 min to form Ge droplets (Solid Phase Epitaxy).

After 4.8 ML Ge deposition on an unpatterned area of the surface, the nanostructures cover homogeneously the surface without lateral ordering, with a density of 4.1×10^{10} islands cm^{-2} (Fig. 29(a)). The size distribution is bimodal with two diameters of 24 and 31 nm. On patterned regions (Fig. 29(b)) Ge droplets, with a density of 3.5×10^{10} islands cm^{-2}, exhibit very good ordering. The diameter distribution displays three peaks, the largest at 47 nm and the other two peaks at 26 and 35 nm. These latter peaks correspond to those obtained on the unpatterned area whereas the 47 nm one is close to the pitch value. These results suggest that patterning favours first of all the formation of nanostructures with the same periodicity of pits, which reach a larger size. Moreover, the shape of the distribution, especially its tail, indicates that a transition toward a larger nanostructure is not yet completed, i.e. the annealing time is not long enough for the Ge droplets to achieve their final equilibrium shape. In Fig. 30 the height

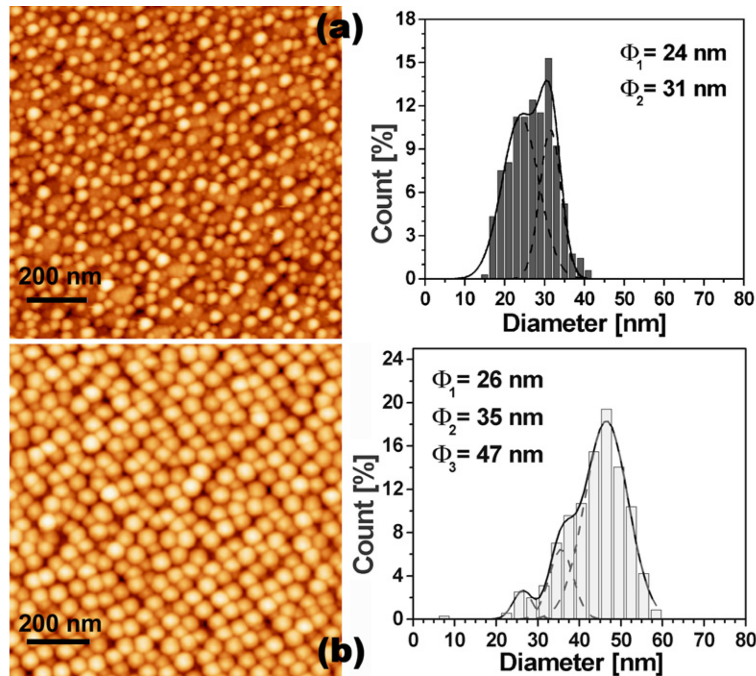

Fig. 29. AFM images (1 μm × 1 μm) after 4.8 ML of Ge deposited at room temperature followed by a thermal annealing at 773 K for 20 min on a 5 nm SiO_2/Si(001) surface; topographs of (a) the unpatterned region and (b) the patterned region with a pitch of 50 nm. On the patterned area the measured average distance between islands is 50.5 ± 0.5 nm, the island diameter is 30.9 ± 0.7 nm, and their height is 9.4 ± 0.6 nm. The corresponding diameter distributions are shown on the right panels.

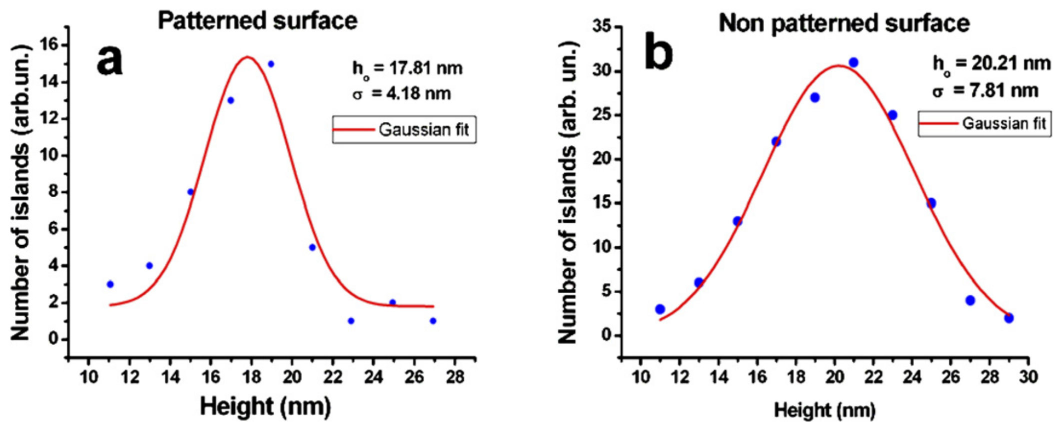

Fig. 30. Height distribution of islands on (a) patterned and (b) non-patterned areas, after deposition of 4.8 ML Ge. The average height on the patterned areas is 17.8 ± 0.2 nm ($\sigma = \text{FWHM} = 4.18$ nm) while on the non-patterned areas the average height is 20.21 nm, and $\sigma = 7.81$ nm.

distribution for the two samples of Fig. 29 is compared. It is evident the narrowing of the Gaussian distribution in the patterned area, confirming that the patterning improves the island uniformity.

10. Conclusions

We have analysed how the nucleation of quantum dots is affected by the surface structure. Starting from the nucleation on ideal surfaces, we have firstly studied the effects of the steps and of their aggregation on the island formation. We have demonstrated that it is possible to control the terrace width on Si(111) by a careful choice of annealing temperature and current direction. When the terraces are wide enough (larger than the mean free path of the atoms on

the surface) the islands nucleate at a constant distance from each other and from the step edges, creating an ordered distribution. The island–island distance can be used as an evaluation of the mean free path of Ge atoms on flat Si(111) terraces.

On vicinal Si(100) surfaces it has been possible to obtain a nanopatterning by using the self organisation of atomic steps. Here the surface create ridges and valleys because of the step meandering when an alloy with low lattice mismatch (Ge_xSi_{1-x}) is deposited. On these rippled SiGe template layers we have organized ultrasmall Ge islands by Sb surfactant-mediated growth of Ge. Since the nucleation of islands occurs only in the surfactant-free surface, the way in which Sb partial coverage is obtained affects the island size and organization, yielding a tool to produce finely ordered small islands. In this process, which is based only on growth steps, the relevant experimental parameters are the Ge concentration of the SiGe alloy, which controls the ripple wavelength and the Sb coverage which controls the island size.

The analysis of InAs epitaxial deposition on GaAs(001) has revealed the localization of precursors at the surface steps. The process begins with the nucleation of very small 3D islands at the upper edge of steps, indicating the presence of a minimum in the potential in proximity of the step edge.

Ge growth on nanopatterned Si(001) surfaces at 773 K has been followed in real time by STM. During the WL formation, Ge atoms do not go inside the pits. Rather, they form new layers, which stop at 1.4 nm from the boundary of the pits. As a consequence, the pit diameter and depth increase with coverage. The growth of a pre-pyramid is characterized by the combination of {105} faceting and stepped morphology. When all parts of a facet are connected, the pyramid grows by developing its four facets. On nanopatterned surfaces, pits act as preferential sites for the nucleation of pre-pyramids. From these results, it appears that STM nanolithography can be exploited to form ordered arrays of Ge islands by choosing a periodic array of pits and taking into account the diffusion of Ge atoms over the collection area.

The FIB patterning of Si and SiO_2 surfaces affect the nucleation sites of Ge nanostructures deposited, increasing both ordering and homogeneity of the islands. A good matching is obtained between the density of the original array of pits (up to 4.3×10^{10} holes·cm^{-2}) and the resulting arrays of Ge droplets. The annealing process reduces the islands size distribution width.

A real time STM study confirms that pyramids nucleate nearby the pits and then, by increasing their size, the island transformed in a dome, covers the pits. From the analysis of the size distribution, we established that a second set of islands develop in between the pits at large coverages, showing that the patterning affects the lateral ordering but not the growth mode. In the case of a SiO_2 surface, patterning drives Ge to form a well ordered array of droplets after thermal annealing. We conclude that the ordered distribution of pits produced by FIB is an efficient template to obtain ordered arrays of QDs. Our results suggest also that it is possible to shrink the size distribution of islands by exploiting the diffusion length of the atoms on the surface, using the right combination of the array pitch and growth temperature. The richness of the results presented evidences the complexity of heteroepitaxy. Nevertheless all analyzed systems show that nucleation taking place at defect sites is dominant over homogeneous nucleation, as predicted by the theory. This result suggests in perspective the possibility of exploiting new nanopatterning strategies using the right match between diffusion length and array pitch.

Acknowledgements

Part of this work was supported by the European Community (EC) through FORUM-FIB contract (IST-2000-29573) at Roma Tor Vergata University. The authors are also indebted to F. Rosei, F. Arciprete, E. Placidi, I. Berbezier, A. Ronda for collaborating at various stages of this research.

References

[1] N. Motta, Journal of Physics—Condensed Matter 14 (35) (2002) 8353.
[2] L. Vescan, T. Stoica, B. Hollander, et al., Applied Physics Letters 82 (20) (2003) 3517.
[3] J. Tersoff, B.J. Spencer, A. Rastelli, et al., Physical Review Letters 89 (19) (2002).
[4] I. Berbezier, A. Ronda, A. Portavoce, Journal of Physics—Condensed Matter 14 (35) (2002) 8283.
[5] C. Teichert, Physics Reports 365 (2002) 335.
[6] T.I. Kamins, G. Medeiros-Ribeiro, D.A.A. Ohlberg, et al., Journal of Applied Physics 85 (2) (1999) 1159.
[7] B. Voigtlander, Surface Science Reports 43 (5–8) (2001) 127.

[8] D.J. Bottomley, Applied Physics Letters 72 (7) (1998) 783.
[9] T. Ishikawa, S. Kohmoto, K. Asakawa, Applied Physics Letters 73 (12) (1998) 1712.
[10] G. Costantini, A. Rastelli, C. Manzano, et al., Applied Physics Letters 85 (23) (2004) 5673;
G. Costantini, A. Rastelli, C. Manzano, et al., Journal of Crystal Growth 278 (1–4) (2005) 38;
G. Costantini, A. Rastelli, C. Manzano, et al., Physical Review Letters 96 (22) (2006).
[11] K. Eberl, M.O. Lipinski, Y.M. Manz, et al., Physica E—Low-Dimensional Systems & Nanostructures 9 (1) (2001) 164.
[12] A. Cazayous, J. Groenen, J. Brault, et al., Physica E—Low-Dimensional Systems & Nanostructures 17 (1–4) (2003) 533.
[13] O.G. Schmidt, A. Rastelli, G.S. Kar, et al., Physica E—Low-Dimensional Systems & Nanostructures 25 (2–3) (2004) 280.
[14] Z.M. Zhao, T.S. Yoon, W. Feng, et al., Thin Solid Films 508 (1–2) (2006) 195.
[15] P. Kratzer, Q.K.K. Liu, P. Acosta-Diaz, et al., Physical Review B 73 (20) (2006).
[16] F. Patella, F. Arciprete, M. Fanfoni, et al., Applied Physics Letters 88 (16) (2006).
[17] H. Mariette, Comptes Rendus Physique 6 (1) (2005) 23.
[18] Y.W. Mo, D.E. Savage, B.S. Swartzentruber, et al., Physical Review Letters 65 (8) (1990) 1020.
[19] A. Vailionis, B. Cho, G. Glass, et al., Physical Review Letters 85 (17) (2000) 3672.
[20] I. Goldfarb, P.T. Hayden, J.H.G. Owen, et al., Physical Review Letters 78 (20) (1997) 3959;
I. Goldfarb, G. Cohen-Taguri, S. Grossman, et al., Physical Review B 72 (7) (2005).
[21] G. Binning, H. Rohrer, C. Gerber, et al., Physical Review Letters 49 (1) (1982) 57.
[22] I.V. Markov, Crystal Growth for Beginners, World Scientific, New York, 1995.
[23] D. Walton, Journal of Chemical Physics 37 (1962) 2182.
[24] G. Zinnsmeister, Thin Solid Films 2 (1968) 497;
G. Zinnsmeister, Thin Solid Films 4 (1969) 3;
G. Zinnsmeister, Thin Solid Films 7 (1971) 51.
[25] R.M. Logan, Thin Solid Films 3 (1969) 59.
[26] M.J. Stowell, T.E. Hutchinson, Thin Solid Films 8 (1971) 41;
M.J. Stowell, T.E. Hutchinson, Thin Solid Films 8 (1971) 411.
[27] D.R. Frankl, J.A. Venables, Advances in Physics 19 (1970) 409.
[28] J.A. Venables, Philosophical Magazine 17 (1973) 697.
[29] R. Vincent, Proceedings of the Royal Society of London, Series A: Mathematical and Physical Sciences 321 (1971) 53.
[30] M. Fanfoni, M. Tomellini, M. Volpe, Applied Physics Letters 78 (2001) 3424.
[31] J.G. Amar, M.N. Popescu, F. Family, Physical Review Letters 86 (2001) 3092.
[32] J.W. Evans, M.C. Bartelt, Physical Review B 66 (2002) 235410.
[33] A. Portavoce, M. Kammler, R. Hull, et al., Nanotechnology 17 (17) (2006) 4451.
[34] E.S. Kim, N. Usami, Y. Shiraki, Applied Physics Letters 72 (13) (1998) 1617.
[35] P.D. Szkutnik, A. Sgarlata, S. Nufris, et al., Physical Review B 69 (20) (2004).
[36] A. Sgarlata, P.D. Szkutnik, A. Balzarotti, et al., Applied Physics Letters 83 (19) (2003) 4002.
[37] M. Tomellini, M. Fanfoni, Surface Science Letters 393 (1997) L99.
[38] H. Omi, T. Ogino, Thin Solid Films 369 (1–2) (2000) 88.
[39] A.V. Latychev, A.L. Aseev, A.B. Krasilninkov, et al., Surface Science 213 (1989) 157.
[40] K. Yagi, H. Minoda, M. Degawa, Surface Science Reports 43 (2001) 45.
[41] H.C. Jeong, E.D. Williams, Surface Science Reports 34 (1999) 171.
[42] J.J. Metois, S. Stoyanov, Surface Science 440 (3) (1999) 407.
[43] F.K. Men, F. Liu, P.J. Wang, et al., Physical Review Letters 88 (9) (2002).
[44] Y. Homma, N. Aizawa, Physical Review B 62 (12) (2000) 8323.
[45] U. Kohler, O. Jusko, G. Pietsch, et al., Surface Science 248 (3) (1991) 321.
[46] W. Seifert, N. Carlsson, M. Miller, et al., Progress in Crystal Growth and Characterization of Materials 33 (4) (1996) 423.
[47] D.E. Jesson, M. Kastner, B. Voigtlander, Physical Review Letters 84 (2) (2000) 330.
[48] F. Boscherini, G. Capellini, L. Di Gaspare, et al., Applied Physics Letters 76 (6) (2000) 682.
[49] F. Rosei, P. Raiteri, Applied Surface Science 195 (1–4) (2002) 16.
[50] L. Vescan, K. Grimm, M. Goryll, et al., Materials Science and Engineering B—Solid State Materials for Advanced Technology 69 (2000) 324.
[51] P.D. Szkutnik, A. Sgarlata, N. Motta, et al., Materials Science & Engineering C 23 (6–8) (2003) 1053.
[52] W.K. Barton, N. Cabrera, F.C. Frank, Philosophical Transactions of the Royal Society of London, Series A: Mathematical and Physical Sciences 243 (1951) 299.
[53] R.L. Schwoebel, E.J. Shipsey, Journal of Applied Physics 37 (1966) 3682.
[54] G.S. Bales, A. Zangwill, Physical Review B 41 (1990) 5500.
[55] D. Kandel, J.D. Weeks, Physical Review Letters 72 (1994) 1678.
[56] J.M. McCoy, J.P. LaFemina, Physical Review B 54 (1996) 14511.
[57] F. Patella, A. Sgarlata, F. Arciprete, et al., Journal of Physics—Condensed Matter 16 (2004) S1503.
[58] F.C. Frank, in: B. Roberts, R. Doremus, D. Turnbull (Eds.), Growth and Perfection of Crystals, Wiley, New York, 1958, p. 511.
[59] D. Kandel, J.D. Weeks, Physical Review B 49 (1994) 5554.
[60] F. Patella, M. Fanfoni, F. Arciprete, et al., Applied Physics Letters 78 (2001) 320;
F. Arciprete, A. Balzarotti, M. Fanfoni, et al., Recent Research Developments in Vacuum Science & Technology 3 (2001) 71.

[61] G.S. Bales, A. Zangwill, Physical Review B 41 (9) (1990) 5500.
[62] I. Berbezier, B. Gallas, L. Lapena, et al., Journal of Vacuum Science & Technology B 16 (1998) 1582.
[63] J. Tersoff, Physical Review B 43 (11) (1991) 9377.
[64] A. Pimpinelli, A. Videcoq, Surface Science 445 (2000) L23.
[65] C. Schelling, M. Mühlberger, G. Springholz, et al., Physical Review B 64 (2001) 41301.
[66] J. Myslivecek, C. Schelling, F. Schaffler, et al., Surface Science 520 (3) (2002) 193.
[67] H. Lichtenberger, M. Mühlberger, F. Schäffler, Applied Physics Letters 86 (13) (2005) 131919.
[68] C. Teichert, J.C. Bean, M.G. Lagally, Applied Physics (a)—Materials Science & Processing 67 (6) (1998) 675.
[69] I. Berbezier, A. Ronda, F. Volpi, et al., Surface Science 531 (3) (2003) 231.
[70] L.W. Guo, N. Lin, Q. Huang, et al., Applied Surface Science 126 (3–4) (1998) 213.
[71] F. Watanabe, D.G. Cahill, S. Hong, et al., Applied Physics Letters 85 (2004) 1238.
[72] I. Berbezier, A. Ronda, A. Portavoce, et al., Applied Physics Letters 83 (23) (2003) 4833.
[73] P.D. Szkutnik, A. Sgarlata, A. Balzarotti, et al., Physical Review B (2006), in press.
[74] X.R. Qin, B.S. Swartzentruber, M.G. Lagally, Physical Review Letters 84 (20) (2000) 4645.
[75] X. Chen, D.K. Saldin, E.L. Bullock, et al., Physical Review B 55 (12) (1997) R7319.
[76] S.M. Lee, E. Kim, Y.H. Lee, et al., Journal of Korean Physical Society 33 (1998).
[77] E. Kim, C.W. Oh, Y.H. Lee, Physical Review Letters 79 (23) (1997) 4621.
[78] Z.Y. Lu, C.Z. Wang, K.M. Ho, Physical Review B 61 (2000) 2329;
J. Wingerden, A. van Dam, M.J. Haye, et al., Physical Review B 55 (7) (1997) 4723.
[79] J.H. Zhu, K. Brunner, G. Abstreiter, Applied Physics Letters 73 (5) (1998) 620.
[80] M. Abdallah, I. Berbezier, P. Dawson, et al., Thin Solid Films 336 (1–2) (1998) 256.
[81] K. Sakamoto, H. Matsuhata, M.O. Tanner, et al., Thin Solid Films 321 (1–2) (1998) 55.
[82] A. Ronda, I. Berbezier, A. Pascale, et al., Materials Science and Engineering B—Solid State Materials for Advanced Technology 101 (1–3) (2003) 95.
[83] A. Portavoce, A. Ronda, I. Berbezier, Materials Science and Engineering B—Solid State Materials for Advanced Technology 89 (1–3) (2002) 205.
[84] A. Portavoce, I. Berbezier, A. Ronda, Materials Science and Engineering B—Solid State Materials for Advanced Technology 101 (1–3) (2003) 181.
[85] T.I. Kamins, R.S. Williams, Applied Physics Letters 71 (9) (1997) 1201.
[86] P. Sutter, P. Zahl, E. Sutter, Applied Physics Letters 82 (20) (2003) 3454.
[87] P. Raiteri, D.B. Migas, L. Miglio, et al., Physical Review Letters 88 (25) (2002).
[88] P. Sutter, I. Schick, W. Ernst, et al., Physical Review Letters 91 (17) (2003).
[89] P. Sutter, M.G. Lagally, Physical Review Letters 84 (20) (2000) 4637.
[90] J. Tersoff, Y.H. Phang, Z. Zhang, et al., Physical Review Letters 75 (1995) 2730.
[91] M. Borgstrom, V. Zela, W. Seifert, Nanotechnology 14 (2003) 264.
[92] T. Schwarz-Selinger, Y.L. Foo, D.G. Cahill, et al., Physical Review B 65 (12) (2002) 125317.
[93] J. Gierak, E. Cambril, M. Schneider, et al., Presented at the 43rd International Conference on Electron, Ion, and Photon Beam Technology and Nanofabrication, Marco Island, Florida (USA), 1999 (unpublished).
[94] F. Patella, A. Sgarlata, F. Arciprete, et al., Journal of Physics—Condensed Matter 16 (17) (2004) S1503.
[95] A. Sgarlata, A. Balzarotti, I. Berbezier, et al., in: IEEE Proceedings of ICONN 2006 Conference, Brisbane, Australia, 2006, in press.
[96] M. Kammler, R. Hull, M.C. Reuter, et al., Applied Physics Letters 82 (7) (2003) 1093.
[97] Z. Zhong, A. Halilovic, M. Mülberger, et al., Journal of Applied Physics 93 (2003) 6256.
[98] F. Ratto, A. Locatelli, S. Fontana, et al., Physical Review Letters 96 (9) (2006).
[99] A. Karmous, A. Cuenat, A. Ronda, et al., Applied Physics Letters 85 (26) (2004) 6401.
[100] D.J. Srolovitz, Acta Metallurgica 37 (1989) 621.
[101] I. Berbezier, A. Karmous, A. Ronda, et al., Journal of Physics: Conference Series 10 (2005) 73.
[102] A.V. Kolobov, A.A. Shklyaev, H. Oyanagi, et al., Applied Physics Letters 78 (17) (2001) 2563.
[103] A.A. Shklyaev, M. Shibata, M. Ichikawa, Physical Review B 62 (3) (2000) 1540.
[104] A. Barski, M. Derivaz, J.L. Rouviere, et al., Applied Physics Letters 77 (22) (2000) 3541.
[105] A.A. Shklyaev, M. Ichikawa, Applied Physics Letters 80 (8) (2002) 1432.
[106] T. Baron, B. Pelissier, L. Perniola, et al., Applied Physics Letters 83 (7) (2003) 1444.
[107] A. Karmous, I. Berbezier, A. Ronda, Physical Review B 73 (7) (2006) 075323.
[108] A. Rastelli, H. von Kanel, Surface Science 515 (2–3) (2002) L493.
[109] P.D. Szkutnik, A. Sgarlata, E. Placidi, et al., Surface Science (2006), in press.